



# Hybrid polyphenolic Network/SPIONs aggregates with potential synergistic effects in MRI applications

A. Lazzarini<sup>a,\*</sup>, R. Colaiezzi<sup>a</sup>, A. Galante<sup>b,c,d</sup>, M. Passacantando<sup>a</sup>, D. Capista<sup>a</sup>, F. Ferella<sup>a,c</sup>, M. Alecci<sup>b,c,d</sup>, M. Crucianelli<sup>a,\*</sup>

<sup>a</sup> Department of Physical and Chemical Sciences, University of L'Aquila, Via Vetoio (COPPITO 1-2), 67100, L'Aquila, Italy

<sup>b</sup> Department of Life, Health and Environmental Sciences, University of L'Aquila, Via Vetoio (COPPITO 2), 67100, L'Aquila, Italy

<sup>c</sup> INFN Gran Sasso National Laboratories, Via G. Acitelli 22, 67100, Assergi (AQ), Italy

<sup>d</sup> Institute for Superconductors, Oxides and Other Innovative Materials and Devices, National Research Council, Via Vetoio 1, 67100, L'Aquila, Italy

## ARTICLE INFO

### Keywords:

Metal-Phenolic Complexes  
Magnetic Nanoparticles  
Contrast Agent  
Ionic Gadolinium

## ABSTRACT

the development of novel and more efficient contrast agents for diagnostic applications is necessary to lower the dosage of such substances that might accumulate in patients with toxic effects and to define new agents which effect could go beyond the simplified scheme of  $T_1$  or  $T_2$  relaxation properties. Within this context, novel directions for MRI contrast agents based on magnetic nanoparticles entrapped inside a polyphenolic network to gain water dispersibility, were explored. Investigation about the possible realization of dual-mode contrast agents chelating  $Gd^{3+}$  ions on the nanoparticles coating, with tunable  $T_1$  and  $T_2$  relaxivity, has been performed. Two synthetic routes were explored, based on covalently bound Tannic Acid (TA) covering magnetic nanoparticles, or PEGylated TA entangling the magnetic systems. Hybrid aggregates having optimal stability in aqueous medium, were characterized through FT-IR, DLS, ICP-MS, XPS, TGA and STEM, confirming the formation of a stable coating around the magnetic nanoparticles, able to carry Gd species. Afterwards, their longitudinal ( $r_1$ ) and transverse ( $r_2$ ) relaxivity values were measured with a 1 T preclinical MRI scanner, as preliminary test for further MRI application. This contribute represents the first step for the preparation of tunable dual-mode contrast agents, with modifiable positive-to-negative contrast according to specific diagnostic needs, aiming to a more patient-tailorable medicinal diagnosis.

## 1. Introduction

It has been few decades since when Super-Paramagnetic Iron Oxide Nanoparticles (SPIONs) have appeared in the chemistry field. They gained more and more attention from the community, thanks to their versatility of application in fields like catalysis [1–5], as well as for biological and biomedical applications [6–11]. In the latter case, they found wide interest, especially as MRI contrast agents [12–16]. This was due to the intrinsic low toxicity level of SPIONs with respect to other contrast media like Gd-based commercial products, widespread in clinical MRI applications. However, dealing with solids (even if with low dimensions), the stability of such systems in physiological conditions (i. e. 36–37 °C, aqueous environment,  $pH \approx 7$ ) is not granted. Therefore, it is necessary to act on the surface of these materials, making them compatible with operating environment. Such variation has to be performed avoiding to negatively alter those magnetic properties that are

crucial for their effectiveness. Surface functionalization in commercially available systems is already performed with bio-compatible polymers, such as dextran and its derivatives [17–20], leading to a stable suspension in aqueous medium. Similar results have been obtained with polyethylene glycol (PEG), through an entanglement effect between magnetic nanoparticles and PEG chains of various lengths [11,21,22]. Even though SPIONs are stably suspended with these functionalization, the ionic Gd-based contrast media remain the preferred option in clinical practice [23–28]. Nevertheless, scientific efforts are directed towards enabling their efficient use with lower dosages, aiming at better results. An optimum for these materials would be obtainable through the combination of the relaxivity effects of either SPIONs or Gd ions, even if the effect that both systems could have on relaxivity, cannot be neglected.

MRI contrast agents are generally classified as positive or negative. Positive ones are also defined as  $T_1$  agents and induce a bright signal by reducing the longitudinal relaxation time. Negative ones, instead, are

\* Corresponding authors.

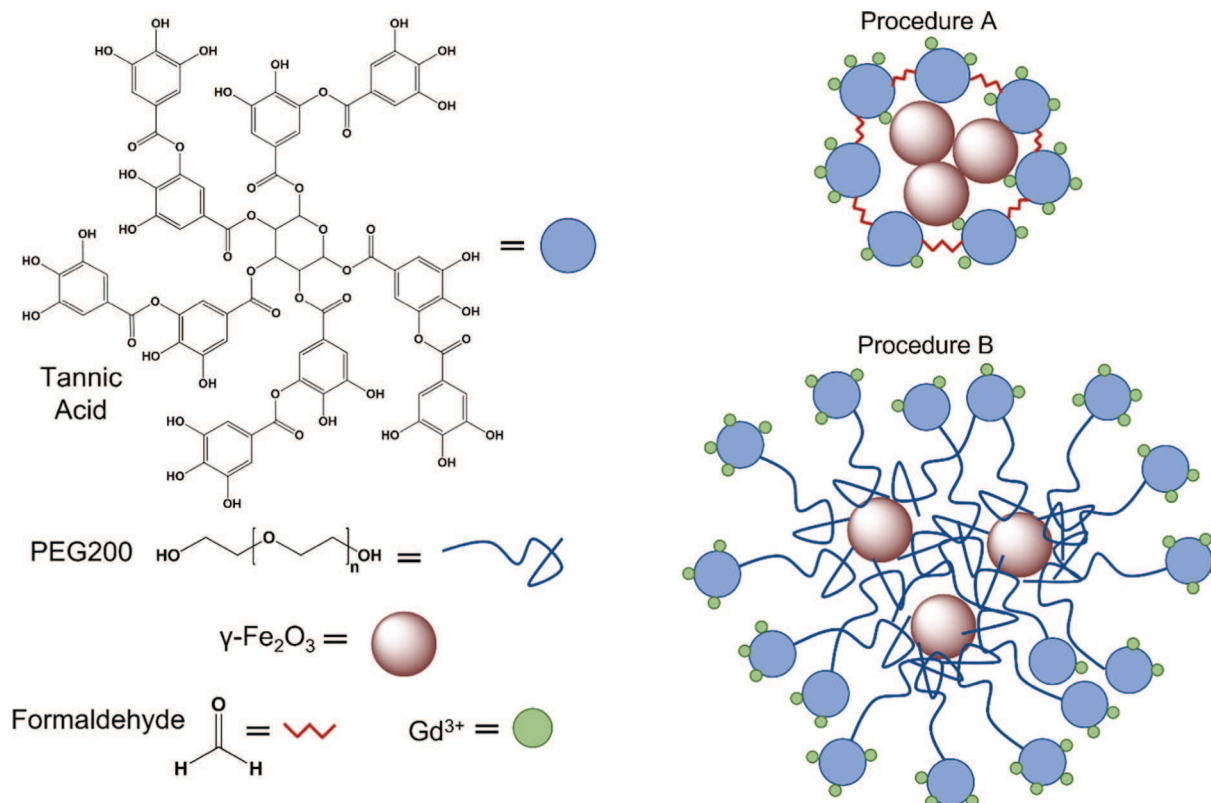
E-mail addresses: [andrea.lazzarini@univaq.it](mailto:andrea.lazzarini@univaq.it) (A. Lazzarini), [marcello.crucianelli@univaq.it](mailto:marcello.crucianelli@univaq.it) (M. Crucianelli).

<https://doi.org/10.1016/j.rechem.2022.100387>

Received 24 March 2022; Accepted 31 May 2022

Available online 2 June 2022

2211-7156/© 2022 The Author(s). Published by Elsevier B.V. This is an open access article under the CC BY license (<http://creativecommons.org/licenses/by/4.0/>).



**Scheme 1.** Reagents (left part) and products expected from the synthetic procedures A (right upper part) and B (right lower part).

defined as  $T_2$  agents and induce a dark signal shortening the transverse relaxation time. The former group is generally based on paramagnetic elements (Gd or Mn ions) while iron oxide particles are often the active element for the latter one. However, this classification can be misleading since any contrast agent reduces both  $T_1$  and  $T_2$ . The outcome on the image intensity depends on the agent relaxivity, the tissue original relaxation times, as well as the experimental procedure. For these reasons, dual-mode  $T_1$ - $T_2$  contrast agents could be beneficial when accurate information is desired [29] and/or to disambiguate image artifacts [30,31]. A contrast agent realized with a single MRI-active element could not solve this problem since it will be characterized by a fixed ratio among the longitudinal and transverse relaxivities. Combined solutions containing either  $T_1$  or  $T_2$  contrast agents could be a possible approach. However, interference among the two can generate unexpected outcomes [32]. A different approach is the design of bimodal  $T_1$ - $T_2$  contrast agents using the appropriately functionalized magnetic nanoparticle, able to host complexes of both categories. This approach was already pursued with magnetoliposomes charged with Gd ions [33],  $\text{Fe}_3\text{O}_4/\text{MnO}$  hybrid nanocrystals [34], Gd labeled SPIONs [35,36]. Our research goes towards this direction, by exploring new coatings for the SPION particles, as well as novel routes to obtain dual-mode tunable MRI contrast agents by anchoring Gd ions to them.

Usually, the polymers employed as iron oxide NPs coating do not possess any anchoring point able to stably coordinate Gd ions. Thus, the scope of this research was to find novel solutions to overcome this problem. The answer might come from a novel class of materials, namely Metal Phenolic Networks (MPNs). MPNs are a category of self-assembly materials able to coat surfaces different in nature (oxides, polymers, 2D materials, cells and bacteria, etc.). They are prepared by mixing together polyphenolic molecule with a trivalent metal ion [37–42]. Generally, Tannic Acid (TA) is the adopted polyphenol to produce MPNs, thanks to its large availability and its extensive number of phenolic units. These features makes it suitable for the formation of supramolecular coordination structures, consisting of different metal

ions and polyphenols units [38]. Such materials have been already used as magnetic supports coating, although with different target applications. Indeed, they have been previously employed as systems able to adsorb and degrade environmental pollutants [43,44], or as catalytic materials [40]. MPNs have also been used for biomedical applications, especially in cancer diagnostics and treatment [45–52]. However, the combination of magnetic nanoparticles coated with metal phenolic networks has never been exploited so far for potential MRI applications. One of the main reasons behind this lack is probably related to MPNs intrinsic fragility, principally due to the change of working pH of the solution [37]. To make such systems more stable, without losing their coordinative properties, two different strategies were adopted. The first one is based on the partial covalent bonding among TA molecules; the second one relies on the controlled TA reticulation with a linear biocompatible polymer. The two synthetic routes (A and B, see onward) should allow to achieve stable phenolic-based systems, able to enhance the effective stability of the coated SPIONs, in aqueous suspensions. On the other hand, hybrid systems should allow the stable coordination of  $\text{Gd}^{3+}$  ions by the organic coating.

The main differences between the synthetic routes are briefly highlighted here. In procedure A, the framework surrounding the magnetic nanoparticles has been created by chemically cross-linking TA molecules by means of formaldehyde in basic environment (TA reticulation). Gd species were added in the formulation, either during the reticulation step or through a post synthetic procedure (samples  $A_n$ ). The anchoring of Gd ions was expected to follow a metal-catechol coordination assembly process (Scheme 1 - Procedure A). In procedure B, TA PEGylation was performed in the presence of SPIONs, according to the Mitsunobu polymerization reaction [53]. In this way, magnetic nanoparticles were entangled within the functionalized polymer chains (PEGylated TA). At this point, the coordination capabilities of the polyphenolic part of the polymer were exploited to anchor Gd species (samples  $B_n$ ) (Scheme 1 - Procedure B).

The two-novel prepared series of samples ( $A_n$  and  $B_n$ ) underwent a

complete physico-chemical characterization, namely FT-IR and X-Ray Photoelectron spectroscopies (XPS), Thermogravimetric Analyses (TGA), electron microscopy (SEM), compositional (ICP-MS) and dimensional (Particle Size Distribution - DLS) analyses. A series of assays were then performed to evaluate their stability in physiological buffer, and their longitudinal ( $r_1$ ) and transverse ( $r_2$ ) relaxivity values were measured. The results herein showed may be viewed as a preliminary overview on the potentiality that such systems possess as contrast agents for Magnetic Resonance Imaging (MRI) applications. Nevertheless, the presented research also aims to move a step forward in the preparation of dual-mode  $T_1$ - $T_2$  contrast agents, going beyond the existing systems. In terms of SPIONs functionalization, the two presented routes are expected to produce completely tailorable systems, able to carry the desired amount of positive/negative agents ratio, without significantly affecting suspension stability. If fully successful, this outcome will represent the first step in the preparation of tunable positive–negative contrast agents, potentially directed to a more patient-oriented medicinal diagnosis.

## 2. Experimental section

### 2.1. Chemicals

Iron trichloride hexahydrate ( $\text{FeCl}_3 \cdot 6\text{H}_2\text{O}$ ), potassium hydroxide (KOH), nitric acid ( $\text{HNO}_3$ ), sodium chloride (NaCl), ammonia solution 30% $_{\text{v/v}}$  ( $\text{NH}_3$ ) and acetonitrile ( $\text{CH}_3\text{CN}$ ) were purchased from Carlo Erba reagents. Diisopropyl azodicarboxylate (DIAD) was purchased from Fluorochem. Fluoridric acid (HF) was purchased by PanReac AppliChem. Tannic Acid (TA), 3-(N-morpholino)propanesulfonic acid (MOPS), trisodium citrate dihydrate were purchased from Alfa Aesar. Sodium acetate, ethylene glycol, anhydrous ethanol (EtOH), formaldehyde solution 37% $_{\text{v/v}}$ , gadolinium(III) nitrate hexahydrate ( $\text{Gd}(\text{NO}_3)_3 \cdot 6\text{H}_2\text{O}$ ), PEG200, triphenyl phosphine ( $\text{PPh}_3$ ) and D9527 dialysis membrane (medium diameter = 27 mm and molecular weight cut-off = 14 kDa) were purchased from Sigma-Aldrich.  $\text{N}_2$  (5.5) was provided by Rivoira.  $\text{H}_2\text{O}$  milliQ (resistivity 18.2  $\text{M}\Omega/\text{cm}$  at 25 °C) was obtained with a Merck-Millipore purification system. All chemicals were employed with no further purification.

### 2.2. SPIONs synthesis

The synthesis of SPIONs is based on an adjusted literature procedure [54], here shortly reported. 1.3 g of  $\text{FeCl}_3 \cdot 6\text{H}_2\text{O}$  and 0.25 g of trisodium citrate were added into a glass autoclave liner with 35 ml of a 9:1 ethylene glycol:ethanol solution, and dissolved using an ultrasound bath. Afterwards, 1.7 g of sodium acetate was added to the solution, and the glass liner inserted in a rotating Parr reactor head. Once the reactor is closed, oxygen was removed by means of 5 washing cycles with  $\text{N}_2$  gas (15 bar each), also checking for any leak. The chamber was filled with 5 bar of nitrogen and let react at 200 °C for 15 h under mechanical stirring. After that, the reaction was allowed to cool at room temperature and the solid was separated by centrifugation at 5000 rpm for 20 min. The obtained sample was washed 3 times with ethanol and 3 more times with 0.02 M NaCl solution, followed by centrifugation at 5000 rpm for 20 min after each washing. The sample was resuspended in ethanol and dried in an oven at 110 °C.

### 2.3. $A_n$ -series samples synthesis

The series of  $A_n$  samples was prepared through a modified literature procedure [55,56], and it's pictured in Scheme 1. In detail, for sample  $A_1$ , 50 mg of SPIONs were inserted in a Schlenk tube with 6.2 ml of deionized water and 1.3 ml of ethanol and resuspended through ultrasound irradiation. Then, 70  $\mu\text{l}$  of ammonia solution were added and the suspension magnetically stirred. Afterwards, 33 mg of tannic acid were added. After 90 min, 65  $\mu\text{l}$  of formaldehyde solution were added and the

suspension was kept under stirring at room temperature (r.t.) for 4 h. Subsequently, 16.5 mg of  $\text{Gd}(\text{NO}_3)_3 \cdot 6\text{H}_2\text{O}$  were dissolved in 350  $\mu\text{l}$  of deionized water, added to the suspension and kept under stirring at r.t. for 24 h. After that, the temperature was risen to 130 °C for 15 h. The reaction was then allowed to cool to r.t. and the solid was separated by centrifugation at 4000 rpm for 40 min. The obtained sample was washed 6 times with deionized water, followed by centrifugation at 4000 rpm for 40 min after each washing. The obtained sample was dried in high vacuum at 60 °C for 8 h.

For sample  $A_2$ , the same preparation procedure of  $A_1$  was employed, skipping the  $\text{Gd}^{3+}$  ions addition that was performed as follows. The synthesized powder was resuspended in 8 ml of deionized water and 16.5 mg of  $\text{Gd}(\text{NO}_3)_3 \cdot 6\text{H}_2\text{O}$  were added; the suspension was kept at r.t. under stirring for 5 h. The solid was separated by centrifugation at 4000 rpm for 40 min. After supernatant removal, it was washed 3 times with deionized water, followed by centrifugation at 4000 rpm for 40 min after each washing. The obtained sample was dried in high vacuum at 60 °C for 8 h. Summarizing, in sample  $A_1$ , Gd precursor was added to the material prior to the reticulation step, while for sample  $A_2$  its addition has been made after the TA crosslinking step.

### 2.4. $B_n$ -series samples synthesis

The synthesis procedure for the series of  $B_n$  samples has been adapted from the literature [57], and it is pictured in Scheme 1. For sample  $B_1$ , 50  $\mu\text{l}$  of PEG200 and 800 mg of  $\text{PPh}_3$  were dissolved in 80 ml of acetonitrile and kept under vigorous stirring over an ice bath. Separately, 1 g of TA and 100 mg of SPIONs were dissolved in 20 ml of acetonitrile and irradiated with ultrasound until complete suspension of the magnetic nanoparticles. Then, the two previously prepared solutions were joined and kept at 0 °C for 10 min. Afterwards, 590  $\mu\text{l}$  of DIAD were added dropwise. The reaction ran for 60 min at 0 °C, then was removed from the ice bath and kept at r.t. for 90 min. Finally, it was brought to 60 °C for additional 90 min. The reaction slurry was transferred inside a centrifuge tube and magnetically decanted. After supernatant removal, three washing cycles with acetonitrile followed by magnetic decantation were performed. The obtained sample was dried at r.t. overnight, followed by 2 h in high vacuum at r.t.

Samples  $B_2$ ,  $B_3$  and  $B_4$ , were prepared as follows: 10 mg of  $B_1$  were suspended in 4.2 ml of MOPS buffer solution (20 mM, pH = 7.4) inside a 10 ml reaction balloon. Then, aqueous solutions of  $\text{Gd}(\text{NO}_3)_3 \cdot 6\text{H}_2\text{O}$  were added to the suspensions (0.444  $\mu\text{mol}_{\text{Gd}}$  in the case of  $B_2$ , 2.22  $\mu\text{mol}_{\text{Gd}}$  in the case of  $B_3$ , 22.2  $\mu\text{mol}_{\text{Gd}}$  in the case of  $B_4$ ) and were kept under vigorous magnetic stirring for 30 min at r.t. The solutions were then transferred inside a dialysis membrane and dialyzed against 210 ml MOPS buffer solution. In the case of  $B_n$  samples, the use of dialysis workup in place of centrifugation is necessary due to the higher fragility of the entangled TA network with respect to the covalently bound one in the  $A_n$  series. The suspension containing the samples were removed from the membrane and stored in sealed vials. Summarizing, sample  $B_1$  was prepared by means of TA PEGylation in presence of SPIONs. Afterwards, portions of  $B_1$  were suspended in aqueous solutions containing different amount of  $\text{Gd}^{3+}$  precursor, obtaining samples  $B_2$ ,  $B_3$ , and  $B_4$ , respectively.

### 2.5. Characterization techniques

#### 2.5.1. Attenuated Total Reflectance-Mid Infrared (ATR-MIR) spectroscopy

FT-IR spectra were collected by means of a PerkinElmer Spectrum Two instrument equipped with an atmospheric UATR Two accessory and a DTGS detector. Each measurement was the average of 8 scans with 4  $\text{cm}^{-1}$  resolution, collected in the 4000–400  $\text{cm}^{-1}$  range.

#### 2.5.2. X-ray Photoelectron Spectroscopy (XPS)

XPS spectra were acquired with a PHI 1257 system, with a working pressure of  $10^{-9}$  Torr, using a non-monochromatized Mg  $K_{\alpha}$  X-ray source

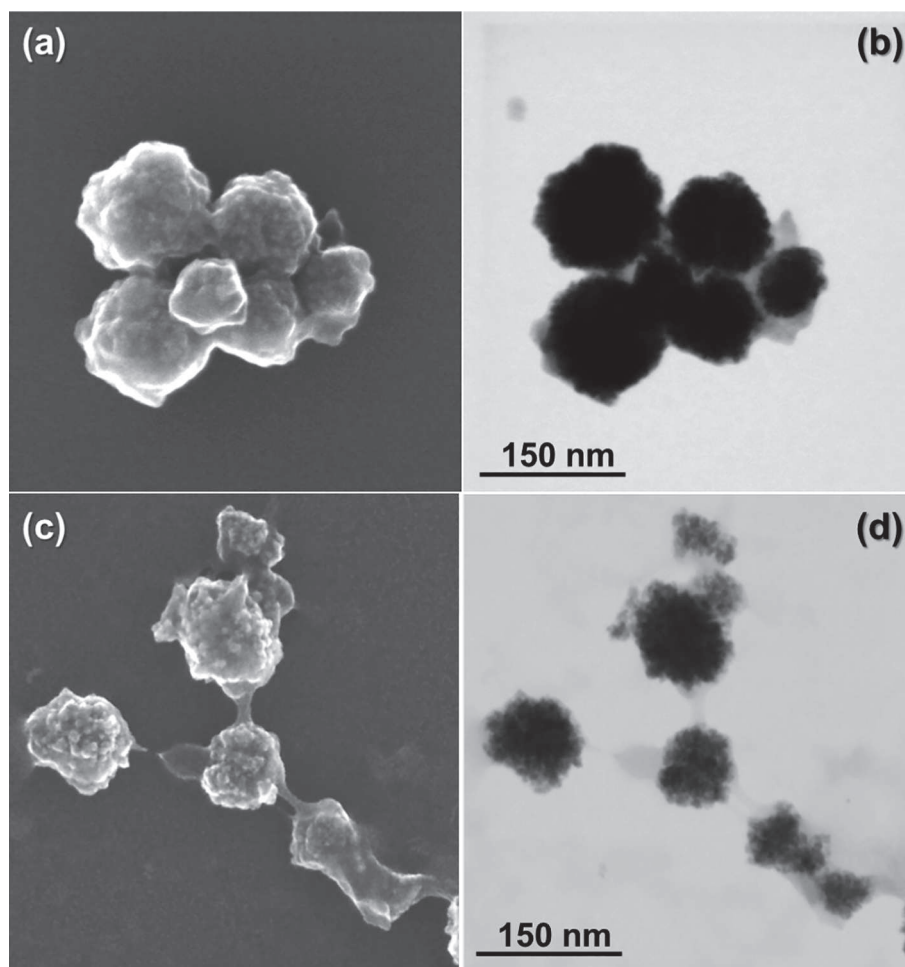


Fig. 1. SEM images collected at 300kx either in transmission (b and d) or with backscattered electrons (a and c) for samples A<sub>1</sub> (a - b) and B<sub>1</sub> (c - d).

and a hemispherical analyzer. C 1s, O 1s, Gd 4d and Fe 2p spectral regions were collected with a constant pass energy of 23 eV, corresponding to a spectral resolution of 0.75 eV. The obtained spectra were aligned exploiting the C 1s peak at 284.8 eV in binding energy (BE - not showed here). Background compensation was performed by means of a Shirley function.

### 2.5.3. Scanning Electron Microscopy (SEM)

SEM images were acquired using a FESEM ZEISS Gemini500 instrument. Images were collected with either transmitted or backscattered electrons, operating with an HT (accelerating voltage) of 20 kV. The samples were dispersed via sonication and a drop of the suspension was deposited on TEM copper grids (200 mesh) covered with an amorphous carbon film.

### 2.5.4. Thermogravimetric Analyses (TGA)

TGA was performed with a Linseis L-81 instrument. The measurements were performed in air with a temperature ramp of 10 °C/min from r.t. to 750 °C.

### 2.5.5. Dynamic Light Scattering (DLS)

Particle size measurements were performed by means of a Nanosight NS300 instrument using a blue laser ( $\lambda = 488$  nm). The samples (0.1 ppm in milliQ water) were injected in the instrument cell with a syringe pump using a flow rate of 50  $\mu$ l/s. Five acquisitions of 60 s are made, each one collecting 25 frames/s. The particle size values were obtained by merging and averaging all the data together.

### 2.5.6. Magnetic Resonance Imaging (MRI) analyses

Prior to MRI measurement, the samples were prepared starting from a mother solution of 30  $\mu$ g/ml in MOPS buffer (20 mM, pH = 7.4). T<sub>1</sub> and T<sub>2</sub> were measured using the mother solution, 4 different dilutions (0.8:1, 0.5:1, 0.3:1, 0.1:1) and the pure buffer.

MRI was performed with a preclinical M3 Aspect Imaging scanner with about 1 T magnetic field (45 MHz). The radiofrequency coil was a solenoid with 3.5 cm inner diameter and 8 cm length, which allowed the insertion of up to six vials with different contrast agent concentration at the same time. T<sub>1</sub> relaxation time was acquired from axial Spin Echo images with FOV of 32x32 mm<sup>2</sup>, 1 mm in-plane resolution and 8 mm slice thickness, T<sub>E</sub> = 4.1 ms and 19 different T<sub>R</sub> values in the 50–10000 ms range for a total acquisition time of 25 min. T<sub>1</sub> was extracted by the exponential recovery of each image voxel intensity, and the values from each vial voxels averaged. The absence of a multi-echo Spin Echo sequence prevented T<sub>2</sub> relaxation determination from images. The use of a Fast Spin Echo sequence with echo train length equal to 192 and all gradients disabled, instead, allowed to effectively perform a whole-sample CPMG acquisition. In this case, multiple echoes from a single vial with T<sub>E</sub> = 4.4 ms and a total measurement time of 2 min were acquired, finally extracting T<sub>2</sub> from the echoes amplitude exponential decay.

### 2.5.7. Inductively Coupled Plasma-Mass Spectrometry (ICP-MS)

ICP-MS analyses were performed with a mass spectrometer Agilent Technologies 7500a equipped with an ASX500 CETAC autosampler. During sequences, a rinsing with HNO<sub>3</sub> 2% solution was carried out to eliminate any memory effect. Mass spectrometer is installed inside ISO-6

**Table 1**

Mean particle size, Gd amount and relaxivity data ( $r_1$  and  $r_2$  parameters) for the  $A_n$  and  $B_n$  series of samples.

Sample name	Particle size (nm) <sup>†</sup>	Gd content (% <sub>w/w</sub> ) <sup>#</sup>	$r_1$ value ( $\frac{ms^{-1}}{\mu g/ml}$ )	$r_2$ value ( $\frac{ms^{-1}}{\mu g/ml}$ )
SPIONs	131.2 ± 4.2	–	2.0•10 <sup>-5</sup> §	4.0•10 <sup>-4</sup> §
A <sub>1</sub>	125.5 ± 3.1	4.57	8.4•10 <sup>-3</sup>	0.97
A <sub>2</sub>	117.9 ± 1.2	0.62	8.7•10 <sup>-3</sup>	1.22
B <sub>1</sub>	141.2 ± 1.2	–	9.1•10 <sup>-3</sup>	1.68
B <sub>2</sub>	124.9 ± 1.8	0.66	14.5•10 <sup>-3</sup>	0.22 §
B <sub>3</sub>	140.8 ± 3.3	2.64	- *	- *
B <sub>4</sub>	127.8 ± 4.6	12.95	- *	- *

<sup>†</sup> Measured with DLS.

<sup>#</sup> Measured with ICP-MS.

§ The sample aggregated during measurements and the trend lost its linearity due to an uncontrolled concentration variation of the aqueous suspension.

\* Values not measurable due to the high instability of the sample in buffer suspension.

clean room to reduce risk of environmental contamination. The procedure for samples solubilization is described in the following part: 4 mg of each sample were weighed in previously conditioned PFA vials. Dissolution of samples was carried out with 1 ml of HNO<sub>3</sub> and 100 µl of HF, heat treated at 120 °C for 60 min. Subsequently, 8 ml of H<sub>2</sub>O were added into PFA vials at 100 °C for additional 60 min. Samples were centrifuged at 4000 rpm for 20 min to remove the supernatant. A second etching was performed with same procedure using 1 ml HNO<sub>3</sub> and 5 ml H<sub>2</sub>O in two different steps of 60 min each. The goal of second etching is related to recouping eventual traces of non-solubilized samples inside the vials. The obtained solutions were united and then diluted 1:50 to performed ICP-MS characterization. Calibration curves to estimate Fe and Gd content are shown in supporting information (Figures S1 and S2 respectively).

### 3. Results and discussion

As previously stated, the metal-catechol coordination assembly process aimed to stabilize aqueous suspensions of SPIONs, was based on two different A and B synthetic procedures. Both procedures were optimized: in the case of route A, different SPIONs/TA and TA/formaldehyde ratios, with different reaction temperatures were tested. For procedure B, instead, different molecular weights intervals for PEG, different PEG/TA ratios, and different reaction temperatures were considered. Herein, for both A and B procedure, only the  $A_n$  and  $B_n$  samples produced under optimized synthetic conditions that guaranteed a good stability in aqueous media, are reported.

The synthetic differences between the two procedures could be reflected in morphological dissimilarity among them. For such reason, scanning electron microscopy (SEM) measurements were performed, either with transmitted or backscattered electrons (Fig. 1). The presence of a more compact texture in the case of the sample A<sub>1</sub> was expected. In this case, the covalent binding between TA molecules surrounding the magnetic nanoparticles create a rigid structure encapsulating them. Fig. 1a shows the complete packing of the particles in sample A<sub>1</sub> and a loop around a small compact group of particles, indicating the formation of a rigid framework surrounding those SPIONs (Fig. 1b). Images of sample B<sub>1</sub> collected with either backscattered (Fig. 1c) or transmitted electrons (Fig. 1d) show a less rigid system. This is evidenced by the distance present among the SPIONs, which are still connected through filaments of PEGylated TA. Comparison of A and B sample images also shows the enhanced superficial smoothness provided by the organic coating.

However, picturing an image for these samples only in a dry environment (as for SEM technique) might draw to misleading conclusions for systems working in the liquid phase. To collect further dimensional

data in liquid phase, thus avoiding any ambiguity, knowing the particle size distribution of all systems in aqueous medium, is mandatory. Such data were obtained by means of dynamic light scattering (DLS) measurements (see Table 1 and Figures S3-S9). For samples  $A_n$ , there are not consistent variations in the mean size of the aggregates, independently whether the addition of Gd<sup>3+</sup> precursor happened before ( $A_1$ ) or after ( $A_2$ ) the reticulation step. Nevertheless, it is possible to observe the formation of small populations of larger aggregates, potentially due to intermolecular H-bonding between TA molecules covering the SPIONs (Figures S4-S5). However, their presence is not affecting samples stability in suspension, which are stable up to several weeks. Despite such similarities in particle dimensions, a large difference in Gd loading for the two procedures (4.6%<sub>w/w</sub> for  $A_1$  vs 0.6%<sub>w/w</sub> for  $A_2$ ) is displayed. Also for  $B_n$  samples, the observed average particle size does not show a clear trend in relation to Gd content. Nonetheless, it is possible to ascribe a certain tendency of the particles towards aggregation with the increase of gadolinium content. In the case of samples B<sub>1</sub> (without Gd - Figure S6) and B<sub>2</sub> (lowest Gd content - Figure S7), particle size populations are pretty homogeneous. Conversely, samples B<sub>3</sub> (intermediate Gd content - Figure S8) and B<sub>4</sub> (highest Gd content - Figure S9) display a certain inhomogeneity in particle size, with the appearance of populations towards much larger dimensions than the average one. It is reasonable to expect that the presence of larger aggregates might possibly have a negative influence on the stability of the system in aqueous suspension. Such effect is potentially related to Gd amount loaded in  $B_n$  samples. Aggregation phenomenon will then tend to reduce the surface-to-bulk ratio of our systems, causing the substantial loss of solubility [58–60].

Apparently, there might also be a negative trend relating  $B_n$  samples stability and Gd content. Indeed, samples without ( $B_1$ ) and with the lowest amount of gadolinium (0.66 %<sub>w/w</sub> -  $B_2$ ) show a long stability in suspension, ending in a shelf life of the particles in aqueous medium up to several weeks. Conversely, samples potentially behaving as positive contrast agents by carrying a higher amount of Gd<sup>3+</sup> ions ( $B_3$ : 2.64 %<sub>w/w</sub>;  $B_4$ : 12.95 %<sub>w/w</sub>), tend to form macroscopic flakes within few minutes after being suspended in aqueous medium.

Besides knowing the amount of Gd present in our materials, it is likewise important to quantitatively evaluate the degree of effective coverage of SPIONs due to the polyphenolic network. This information is pivotal to understand the way Gd ions could be possibly loaded in our materials. Such quantity has been measured via thermogravimetric analyses (TGA - Figure S10). Concerning the synthetic route A, sample A<sub>1</sub> suffered a weight loss of 19.5 %, while sample A<sub>2</sub> had a weight reduction of 10.5 % (net of initial water loss). It is important to notice that the amount of initial water contained in the two samples is quite similar (7.5 % for A<sub>1</sub> vs 8.1 % for A<sub>2</sub>). Furthermore, after the degradation of the organic component a plateau is reached. Therefore, there is no evidence for the formation of a condensed hydroxylated Gd phase, such as Gd(OH)<sub>3</sub>. Indeed, its presence could have altered either the initial hydration level or given rise to further weight loss above 430 °C [61,62]. In addition, their nature appears quite similar as evidenced by the same final temperature for organic degradation (430 °C). Hence, further investigations are needed to unravel the nature of condensed Gd species potentially present in  $A_n$  samples. Compared to them, sample B<sub>1</sub> had a weight reduction of 13.6 % (net of initial water loss). Despite the difference in terms of organic content, what emerges about the final degradation temperature is crucial. For sample B<sub>1</sub>, in which TA molecules are PEGylated and wrapped around SPIONs by entanglement effect, degradation process terminates close to 380 °C, quite lower than for  $A_n$ . This evidence is the first step to understand the nature of the coating (stronger in the  $A_n$  series with respect to  $B_n$ ) generated around the magnetic nanoparticles.

Once the amount of organic layer coating and the amount of Gd carried by each sample have been determined, the influence on water relaxation time T<sub>1</sub> and T<sub>2</sub> of the samples suspended in physiological buffer, was measured. All the samples were suspended in a 20 mM MOPS buffer solution at physiological pH (7.4), with a concentration of 30 µg/

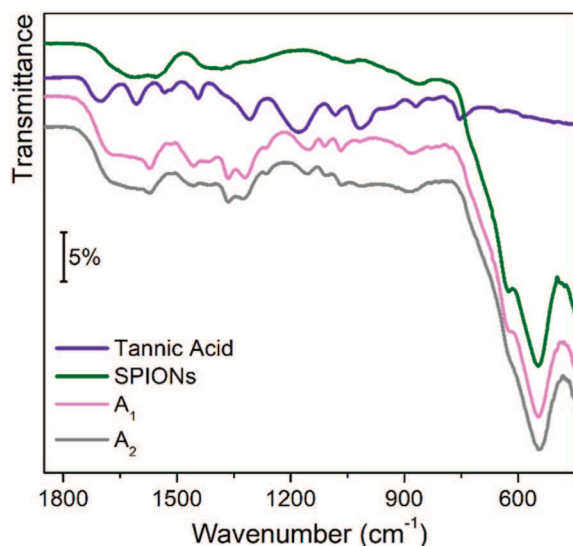


Fig. 2. Normalized ATR-IR spectra in the 1850–450  $\text{cm}^{-1}$  range for samples  $A_1$  (pink curve) and  $A_2$  (grey curve) compared to their precursors, namely SPIONs (green curve) and TA (violet curve). Spectra are shifted for a better comparison.

ml. At this point, the first drawback with the samples has emerged. As previously stated, samples  $B_3$  and  $B_4$  are not stable in suspension. Indeed, after 30 min from the redispersion, both samples display aggregates visible by naked eye, making impossible the relaxivity measurements for these samples. Concerning samples  $A_1$ ,  $A_2$ ,  $B_1$ , and  $B_2$ , they were shelf stable up to several weeks at the highest concentrations. Therefore, they were diluted according to the proportions reported in Section 2, namely 0.8:1, 0.5:1, 0.3:1 and 0.1:1, with respect to the mother solutions. In this way, it was possible to measure the relaxation times with different concentrations. The relaxivity parameters  $r_1$  and  $r_2$ , namely the slope of the lines interpolating the data in the graphs  $1/T_1$  or  $1/T_2$  vs concentration, were obtained (see Figures S11–S15). Samples  $A_1$  and  $A_2$  show two distinct behaviors in relaxivity parameters. Indeed, their influence on  $T_2$  is much larger than on  $T_1$ , while for a  $\text{Gd}^{3+}$  salt these two values are generally quite close to each other [63].  $r_1$  and  $r_2$  values for either  $A_1$  or  $A_2$  differ by almost two orders of magnitude, thus resembling the behavior of commercially available coated SPIONs [64]. In fact, such systems are characterized by a strong  $T_2$  effect, due to the magnetic field inhomogeneities generated by superparamagnetic particles. This could drive the conclusion that the form in which Gd is present in samples  $A_1$  and  $A_2$  is not useful to influence the water relaxivities, i.e. as isolated  $\text{Gd}^{3+}$  ions, but in some other aggregate form. Their formation may be ascribed to the synthetic procedure A, in which high temperature and basic environment were employed, namely the same conditions in which metal oxide nanoparticles are commonly prepared. Nevertheless, this event has been observed for sample  $A_1$  only, in which Gd is added prior to the reticulation step. On the other hand, the lower amount of Gd in sample  $A_2$  with respect to  $A_1$  might reveal an additional phenomenon standing behind its poor performances, as clarified from FT-IR analysis.

FT-IR spectra of  $A_1$  and  $A_2$  (Fig. 2) display a strong reduction of phenolic hydroxyls peak ( $\delta_{\text{ph}}(\text{O-H})$  signal at  $\sim 1200 \text{ cm}^{-1}$ ), with respect to TA [65,66]. This confirms that the crosslinking process, mediated by formaldehyde, occurs via water elimination and the consequent formation of  $-\text{CH}_2-$  bonds, between phenyl units [55,56]. However, crosslinking could not explain completely the Ph-OH elimination process. Indeed, TA catechol units may also be converted into cyclic acetals via acetalization process in the presence of formaldehyde at high temperature, thus enhancing the hydroxyls derivatization of TA phenolic units [67]. The large occurrence of these phenomena could contribute to the depletion of anchoring points for  $\text{Gd}^{3+}$  ions, thus limiting its effect on  $r_1$  relaxivity, in the case of sample  $A_2$ .

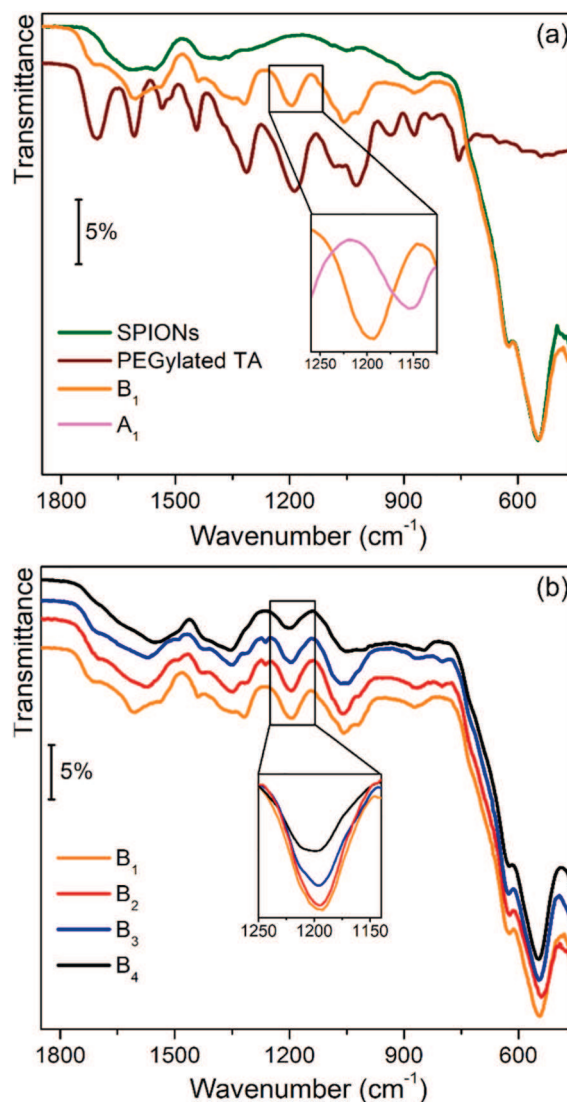
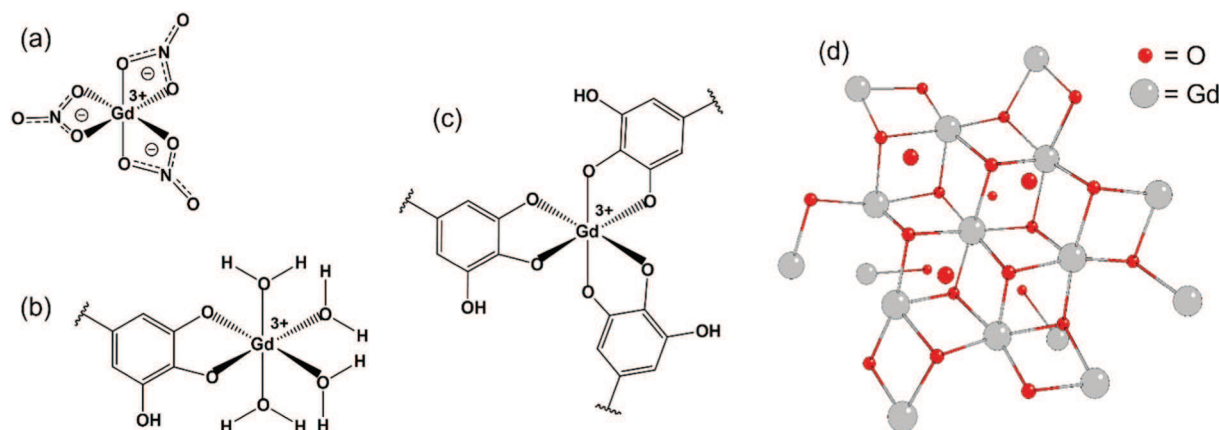
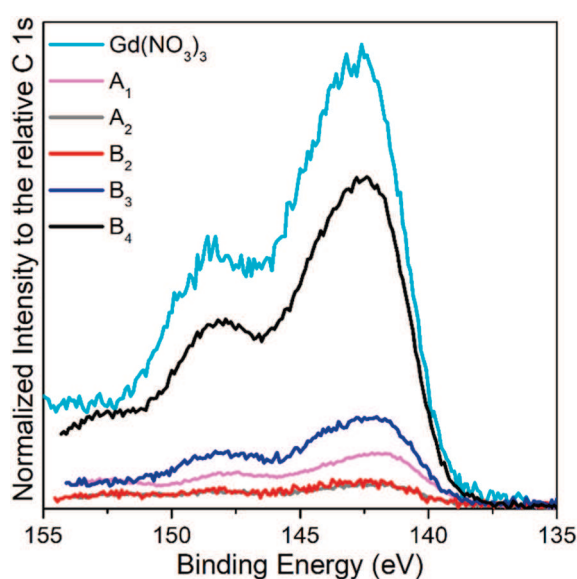


Fig. 3. Part a: normalized ATR-IR spectra in the 1850–450  $\text{cm}^{-1}$  range for sample  $B_1$  (orange curve) compared to its precursors, namely SPIONs (green curve) and PEGylated TA (brown curve); inset highlights the spectral region for  $\delta_{\text{ph}}(\text{O-H})$  vibrations of phenolic species relative to samples  $A_1$  (pink curve) and  $B_1$  (orange curve). Part b: ATR-IR spectra in the 1850–450  $\text{cm}^{-1}$  range for samples  $B_1$  (orange curve),  $B_2$  (red curve),  $B_3$  (blue curve) and  $B_4$  (black curve); inset highlights the spectral region for  $\delta_{\text{ph}}(\text{O-H})$  vibrations of phenolic species for the  $B_n$  series. Spectra in the main figures are vertically shifted for a better comparison, spectra in the insets are not shifted.

Concerning the other synthetic procedure, relaxivities measurements for sample  $B_1$  (having no gadolinium loaded) seem to confirm the hypothesis that only magnetic nanoparticles are influencing relaxivity. Indeed,  $r_1$  and  $r_2$  parameters resemble the ones of pure SPIONs, similarly to  $A_1$  and  $A_2$ . Sample  $B_2$ , instead, reveals hints of Gd presence in isolated form. Even with a minimum loading (0.66 % $_{\text{w/w}}$ ), an increase of almost 50 % for  $r_1$  value, with respect to sample  $B_1$ , has been recorded (see Table 1). However, in the subsequent  $T_2$  measurements,  $r_2$  value was reduced with respect to all other samples, due to a total loss of data linearity (Figure S15). This appears to be the clue of a SPION aggregation process that occurs as a consequence of prolonged exposure of the sample to magnetic fields. When inter-particle magnetic forces increase their intensities, they push together sample particles that, in a situation of closer vicinity, might interact. This is confirmed by the post-MRI observation of aggregates inside the vials containing the most concentrated solutions, which appeared no longer stable in suspension. Such



**Scheme 2.** Schematic representation of the hypothesized Gd local environment in the case of  $\text{Gd}(\text{NO}_3)_3$  (a);  $\text{B}_n$  in low coordination (b);  $\text{B}_n$  in high coordination (c);  $\text{Gd}_2\text{O}_3$  crystal structure, possibly describing the local environment of Gd for samples  $\text{A}_n$  (d).



**Fig. 4.** Gd 4d XPS spectra for  $\text{Gd}(\text{NO}_3)_3$  (light blue), and for samples  $\text{A}_1$  (pink),  $\text{A}_2$  (grey),  $\text{B}_2$  (red),  $\text{B}_3$  (blue),  $\text{B}_4$  (black). All the curves have been aligned to C 1s signal at 284.8 eV and their intensity was normalized according to the same peak (Figure S17a).

aggregates reduce the water-particles surface area, available for water-hydrogen magnetic interactions, and can be responsible of reduced relaxivities. A validation of this hypothesis can be drawn analyzing the signals detected with ATR-MIR spectroscopy for  $\text{B}_n$  samples. In the inset of Fig. 3a, it is possible to observe the difference in  $\delta_{\text{ph}}(\text{OH})$  intensity between samples  $\text{A}_1$  and sample  $\text{B}_1$ . While in the first one the phenolic hydroxyls were almost completely used for the sake of TA reticulation, in the second one the synthetic procedure leaves them almost unaltered and able to serve as anchoring points for  $\text{Gd}^{3+}$  ions. Furthermore, in Fig. 3b,  $\delta_{\text{ph}}(\text{OH})$  signal decreases noticeably with the increase of gadolinium loading (see inset). For sample  $\text{B}_2$ , a Gd local environment similar to the one represented in Scheme 2b, have been hypothesized. In such configuration, the coordination sphere of the metal is only partially saturated by the phenolate bidentate ions. However, the loaded metal is pretty oxophilic and characterized by a large coordination sphere. Hence, in the presence of a high Gd loading and/or high concentrations of phenolic groups, various coated particles endowed with polyphenolic arms will start to interact with each other, under the templating effect of  $\text{Gd}^{3+}$  ion (Scheme 2c). Once a critical dimensions are reached, they will cause a precipitation phenomenon. This might explain the behavior

observed with  $\text{B}_3$  and  $\text{B}_4$  samples. A similar situation in the case of sample  $\text{B}_2$ , could appear after the material has been subjected to a strong magnetic field, as during relaxivity measurements. The magnetic force could have pushed together  $\text{B}_2$  particles to such an extent able to cause particles interaction and precipitation.

To confirm this hypothesis, a careful investigation of Gd local coordination environment and its prevalent oxidation state by means of XPS measurements, is needed (Fig. 4). Indeed, it is known that TA, among others, has also been used as reducing agent in the sustainable synthesis of different metal nanoparticles [44,68]. Such activity, potentially leading to a reduction of Gd species and a total loss of its relaxivity, should be avoided. Since isolated  $\text{Gd}^{3+}$  ions are among the most active species for imaging contrast applications, it is of pivotal importance excluding this side-reaction.

The likely formation of a Gd precipitate, possibly in the form of  $\text{Gd}_2\text{O}_3$ , have been previously hypothesized in the case of  $\text{A}_n$  samples. Peaks position, relative to Gd  $4d_{5/2}$  binding energy at 142 eV and to Gd  $4d_{3/2}$  at 148 eV, confirm the presence of oxidic clusters [69–72]. Indeed, the binding energy associated to the same emission from a metallic zerovalent Gd species is almost 2 eV lower [73], thus excluding any reducing effect of TA. Contemporarily, it is also possible to exclude the presence of  $\text{Gd}(\text{OH})_3$ , since its  $4d_{5/2}$  and  $4d_{3/2}$  XPS signals are at 141.5 and 147.5 eV respectively [74]. However, the formation of oxidic precipitates is the consequence of a two-step process, potentially taking place during the synthetic route A. Such process starts with the formation of a  $\text{Gd}(\text{OH})_3$  precursor in the presence of a basic environment and high temperature [61,75,76], followed by a dehydration step at  $T > \text{r.t.}$  The last step reduces Gd coordination number, changing from 9 (in the case of hydroxide) to 6 (in the case of the oxide) [77], thus leaving only  $\text{Gd}_2\text{O}_3$  as final product.

Comparing this datum with the value for Gd  $4d_{5/2}$  binding energy of  $\text{Gd}(\text{NO}_3)_3$  (~143 eV) [78], it is possible to conclude that the surrounding environment of Gd atoms is pretty similar. In fact, in gadolinium oxide the metal atoms may interact with up to six oxygen atoms in the first coordination shell (Scheme 2d) [77,79]. Similarly,  $\text{Gd}^{3+}$  ions in the nitrate salt are coordinated by six oxygen atoms in the first shell (Scheme 2a) [80]. Samples  $\text{B}_2$ ,  $\text{B}_3$  and  $\text{B}_4$ , for which a situation as the ones in Scheme 2b-c have been pictured, show a Gd  $4d_{5/2}$  band pretty similar to all the other samples. On one hand, the presence of gadolinium species is confirmed to be associated only to the (III) oxidation state. This should influence the relaxivity of the system, similarly to  $\text{Gd}^{3+}$  isolated ions (as in the case of  $\text{B}_2$ ). On the other hand, with the techniques employed so far, it is not possible to clearly distinguish the diverse Gd local environments, since in all the samples Gd is always surrounded by six oxygen atoms.

#### 4. Summary

In this paper, two methodologies capable to stably suspend SPIONs in physiological environment, alternative to the commercially available ones, were optimized. The prepared materials can be considered a preliminary step for the preparation of new hybrid systems for MRI applications, by coupling the coating/entanglement effect of bio-compatible polymers (responsible for the solubility) with chemical species able to bear  $Gd^{3+}$  ions, thus conferring dual modal MRI responsiveness. Both synthetic routes were able to provide a set of samples stable in physiological conditions, capable of carrying Gd species to a certain extent. However, the sample that is most positively affected by the presence of  $Gd^{3+}$  ions ( $B_2$ ), is also the one displaying the lowest operational stability. Contrarywise, the other stable samples do not show appreciable deviation from pure SPIONs relaxivity behavior, despite some of them are loaded with a non-negligible amount of Gd ( $A_1$ ). Nevertheless, they possess elevated stability also after being exposed to intense magnetic fields. The right balance between  $T_1$ - $T_2$  tunability and stability is far to be achieved at the moment. However, a way for further development of new and alternative routes to stably suspend magnetic nanoparticles to be employed as potential dual-mode  $T_1$ - $T_2$  contrast agents has been opened. With the right experimental adjustments, we strongly believe that exploitation of synergic SPIONs and Gd relaxivities effects, for tailored MRI applications, will be available soon.

#### Declaration of Competing Interest

The authors declare that they have no known competing financial interests or personal relationships that could have appeared to influence the work reported in this paper.

#### Acknowledgements

We thank University of L'Aquila and "Fondazione Carispaq" for their financial support.

#### Appendix A. Supplementary data

Supplementary data to this article can be found online at <https://doi.org/10.1016/j.rechem.2022.100387>.

#### References

- [1] D. Lopez-Tejedor, R. Benavente, J.M. Palomo, Iron nanostructured catalysts: design and applications, *Catal. Sci. Technol.* 8 (7) (2018) 1754–1776.
- [2] D. Wang, D. Astruc, Fast-Growing Field of Magnetically Recyclable Nanocatalysts, *Chem. Rev.* 114 (14) (2014) 6949–6985.
- [3] M.B. Gawande, P.S. Branco, R.S. Varma, Nano-magnetite ( $Fe_3O_4$ ) as a support for recyclable catalysts in the development of sustainable methodologies, *Chem. Soc. Rev.* 42 (2013) 3371–3393.
- [4] A. Lazzarini, R. Colaiezzi, M. Passacantando, F. D'Orazio, L. Arrizza, F. Ferella, M. Crucianelli, Investigation of physico-chemical and catalytic properties of the coating layer of silica-coated iron oxide magnetic nanoparticles, *J. Phys. Chem. Solids* 153 (2021), 110003.
- [5] R. Colaiezzi, A. Lazzarini, F. Ferella, V. Paolucci, A. Di Giuseppe, M. Crucianelli, Catalytic Oxygen Atom Transfer promoted by tethered Mo(VI) diiodo complexes onto Silica-Coated Magnetic Nanoparticles, *Inorg. Chim. Acta* 531 (2022), 120711.
- [6] S. Laurent, D. Forge, M. Port, A. Roch, C. Robic, L.V. Elst, R.N. Muller, Magnetic iron oxide nanoparticles: Synthesis, stabilization, vectorization, physicochemical characterizations, and biological applications, *Chem. Rev.* 108 (2008) 2064–2110.
- [7] N. Lee, D. Yoo, D. Ling, M.H. Cho, T. Hyeon, J. Cheon, Iron Oxide Based Nanoparticles for Multimodal Imaging and Magnetoresponsive Therapy, *Chem. Rev.* 115 (19) (2015) 10637–10689.
- [8] E.K. Lim, T. Kim, S. Paik, S. Haam, Y.M. Huh, K. Lee, Nanomaterials for Theranostics: Recent Advances and Future Challenges, *Chem. Rev.* 115 (2015) 327–394.
- [9] A. Avasthi, C. Caro, E. Pozo-Torres, M. Pernia Leal, M.L. García-Martín, Magnetic Nanoparticles as MRI Contrast Agents, *Top. Curr. Chem.* 378 (2020) 40.
- [10] S. Caspani, R. Magalhães, J.P. Araújo, C. Tavares Sousa, Magnetic Nanomaterials as Contrast Agents for MRI, *Materials* 13 (2020) 2586.
- [11] N.R. Nelson, J.D. Port, M.K. Pandey, Use of Superparamagnetic Iron Oxide Nanoparticles (SPIONs) via Multiple Imaging Modalities and Modifications to Reduce Cytotoxicity: An Educational Review, *J. Nanotheranostics* 1 (2020) 105–135.
- [12] A. Antonelli, M. Magnani, SPIO nanoparticles and magnetic erythrocytes as contrast agents for biomedical and diagnostic applications, *J. Magn. Magn. Mater.* 541 (2022), 168520.
- [13] M.I. Khan, M.I. Hossain, M.K. Hossain, M.H.K. Rubel, K.M. Hossain, A.M.U. B. Mahfuz, M.I. Anik, Recent Progress in Nanostructured Smart Drug Delivery Systems for Cancer Therapy, A Review, *ACS Appl. Bio Mater.* 5 (3) (2022) 971–1012.
- [14] M. Khalid Hossain, M. Ishak Khan, A. El-Denglawey, A review on biomedical applications, prospects, and challenges of rare earth oxides, *Appl. Mater. Today* 24 (2021), 101104.
- [15] M.I. Anik, M.K. Hossain, I. Hossain, A.M.U.B. Mahfuz, M.T. Rahman, I. Ahmed, Recent progress of magnetic nanoparticles in biomedical applications: A review, *Nano Select* 2 (6) (2021) 1146–1186.
- [16] M.I. Anik, M. Khalid Hossain, I. Hossain, I. Ahmed, R.M. Doha, Biomedical applications of magnetic nanoparticles in "Magnetic Nanoparticle-Based Hybrid Materials: Fundamentals and Applications"; A. Ehrmann, T.A. Nguyen, M. Ahmadi, A. Farmani, P. Nguyen-Tri Eds.; Woodhead Publishing: Duxford (UK), 2021; pp. 463–497.
- [17] F. Ludwig, T. Wawrzik, T. Yoshida, N. Gehrke, A. Briel, D. Eberbeck, M. Schilling, Optimization of Magnetic Nanoparticles for Magnetic Particle Imaging, *IEEE Trans. Magn.* 48 (11) (2012) 3780–3783.
- [18] B.B. Frericks, F. Wacker, C. Loddenkemper, S. Valdeig, B. Hotz, K.J. Wolf, B. Misselwitz, A. Kuhl, J.C. Hoffmann, Magnetic Resonance Imaging of Experimental Inflammatory Bowel Disease: Quantitative and Qualitative Analyses With Histopathologic Correlation in a Rat Model Using the Ultrasmall Iron Oxide SHU 555 C, *Invest. Radiol.* 44 (2009) 23–30.
- [19] C. Bremer, T. Allkemper, J. Baermig, P. Reimer, RES-specific imaging of the liver and spleen with iron oxide particles designed for blood pool MR-angiography, *J. Magn. Reson. Imaging* 10 (3) (1999) 461–467.
- [20] T. Persigehl, R. Bieker, L. Matuszewski, A. Wall, T. Kessler, H. Kooijman, N. Meier, W. Ebert, W.E. Berdel, W. Heindel, R.M. Mesters, C. Bremer, Antiangiogenic tumor treatment: Early noninvasive monitoring with USPIO-enhanced MR imaging in mice, *Radiology* 244 (2007) 449–456.
- [21] D. Liu, W. Wu, J. Ling, S. Wen, N. Gu, X. Zhang, Effective PEGylation of Iron Oxide Nanoparticles for High Performance In Vivo Cancer Imaging, *Adv. Funct. Mater.* 21 (8) (2011) 1498–1504.
- [22] A.K. Gupta, S. Wells, Surface-modified superparamagnetic nanoparticles for drug delivery: Preparation, characterization, and cytotoxicity studies, *IEEE Trans. Nanobiosci.* 3 (1) (2004) 66–73.
- [23] S. Suarez-García, R. Solorzano, F. Novio, R. Alibes, F. Busque, D. Ruiz-Molina, Coordination polymers nanoparticles for bioimaging, *Coord. Chem. Rev.* 432 (2021), 213716.
- [24] P. Hermann, J. Kotek, V. Kubíček, I. Lukeš, Gadolinium(III) complexes as MRI contrast agents: ligand design and properties of the complexes, *Dalton Trans.* 10.1039/B719704G (2008) 3027–3047.
- [25] R. Jessome, Hyperintensity in the Dentate Nucleus on Nonenhanced T1-Weighted Magnetic Resonance Imaging Suggests Dechelation of Contrast Agents, *J. Med. Imaging Radiat. Sci.* 47 (1) (2016) 86–91.
- [26] T. Ota, J. Kimura, T. Ishiguchi, Safety and clinical usefulness of gadoteric acid including post-marketing surveillance, *Imaging Med.* 4 (4) (2012) 397–409.
- [27] L.J. Scott, Gadobutrol: A Review of Its Use for Contrast-Enhanced Magnetic Resonance Imaging in Adults and Children, *Clin. Drug Invest.* 33 (2013) 303–314.
- [28] W.J. Moon, Y.A. Cho, S. Hahn, H.M. Son, S.K. Woo, Y.H. Lee, The Pattern of Use, Effectiveness, and Safety of Gadoteric Acid (Clariscan) in Patients Undergoing Contrast-Enhanced Magnetic Resonance Imaging: A Prospective, Multicenter, Observational Study, *Contrast Media Mol. Imaging* 2021 (2021).
- [29] M. De, S.S. Chou, H.M. Joshi, V.P. Dravid, Hybrid magnetic nanostructures (MNS) for magnetic resonance imaging applications, *Adv. Drug Deliv. Rev.* 63 (14–15) (2011) 1282–1299.
- [30] Y.B. Kim, K.H. Bae, S.-S. Yoo, T.G. Park, HyunWook Park, Positive contrast visualization for cellular magnetic resonance imaging using susceptibility-weighted echo-time encoding, *Magn. Reson. Imaging* 27 (5) (2009) 601–610.
- [31] J. Zhuo, R.P. Gullapalli, AAPM/RSNA physics tutorial for residents - MR artifacts, safety, and quality control, *Radiographics* 26 (1) (2006) 275–297.
- [32] J.-S. Choi, J.-H. Lee, T.-H. Shin, H.-T. Song, E.Y. Kim, J. Cheon, Self-Confirming "AND" Logic Nanoparticles for Fault-Free MRI, *J. Am. Chem. Soc.* 132 (32) (2010) 11015–11017.
- [33] M. De Cuyper, S.J.H. Soenen, K. Coenegrachts, L. Ter Beek, Surface functionalization of magnetoliposomes in view of improving iron oxide-based magnetic resonance imaging contrast agents: Anchoring of gadolinium ions to a lipophilic chelate, *Anal. Biochem.* 367 (2007) 266–273.
- [34] G.H. Im, S.M. Kim, D.-G. Lee, W.J. Lee, J.H. Lee, I.S. Lee,  $Fe_3O_4$ /MnO hybrid nanocrystals as a dual contrast agent for both  $T_1$ - and  $T_2$ -weighted liver MRI, *Biomaterials* 34 (8) (2013) 2069–2076.
- [35] K.H. Bae, Y.B. Kim, Y. Lee, JinYoung Hwang, HyunWook Park, T.G. Park, Bioinspired Synthesis and Characterization of Gadolinium-Labeled Magnetite Nanoparticles for Dual Contrast  $T_1$ - and  $T_2$ -Weighted Magnetic Resonance Imaging, *Bioconjugate Chem.* 21 (3) (2010) 505–512.
- [36] A. Szpak, S. Fiejdasz, W. Prendota, T. Straczek, C. Kapusta, J. Szymd, M. Nowakowska, S. Zapotoczny,  $T_1$ - $T_2$  Dual-modal MRI contrast agents based on superparamagnetic iron oxide nanoparticles with surface attached gadolinium complexes, *J. Nanopart. Res.* 16 (2014) 2678.

- [37] H. Ejima, J.J. Richardson, K. Liang, J.P. Best, M.P. van Koevorden, G.K. Such, J. Cui, F. Caruso, One-Step Assembly of Coordination Complexes for Versatile Film and Particle Engineering, *Science* 341 (6142) (2013) 154–157.
- [38] J. Guo, Y. Ping, H. Ejima, K. Alt, M. Meissner, J.J. Richardson, Y. Yan, K. Peter, D. vonElverfeldt, C.E. Hagemeyer, F. Caruso, Engineering Multifunctional Capsules through the Assembly of Metal-Phenolic Networks, *Angew. Chem.-Int. Edit.* 53 (22) (2014) 5546–5551.
- [39] H. Ejima, J.J. Richardson, F. Caruso, Metal-phenolic networks as a versatile platform to engineer nanomaterials and biointerfaces, *Nano Today* 12 (2017) 136–148.
- [40] X. Jia, J. Wu, K.e. Lu, Y. Li, X. Qiao, J. Kaelin, S. Lu, Y. Cheng, X. Wu, W. Qin, Organic-inorganic hybrids of Fe-Co polyphenolic network wrapped Fe<sub>3</sub>O<sub>4</sub> nanocatalysts for significantly enhanced oxygen evolution, *J. Mater. Chem. A* 7 (23) (2019) 14302–14308.
- [41] T. Zeng, X.L. Zhang, Y.Y. Guo, H.Y. Niu, Y.Q. Cai, Enhanced catalytic application of Au@polyphenol-metal nanocomposites synthesized by a facile and green method, *J. Mater. Chem. A* 2 (2014) 14807–14811.
- [42] J. Guo, B.L. Tardy, A.J. Christofferson, Y. Dai, J.J. Richardson, W. Zhu, M. Hu, Y. i. Ju, J. Cui, R.R. Dagastine, I. Yarovsky, F. Caruso, Modular assembly of superstructures from polyphenol-functionalized building blocks, *Nature Nanotech.* 11 (12) (2016) 1105–1111.
- [43] Y. Qian, S. Chen, C. He, C. Ye, W. Zhao, S. Sun, Y.i. Xie, C. Zhao, Green Fabrication of Tannic Acid-Inspired Magnetic Composite Nanoparticles toward Cationic Dye Capture and Selective Degradation, *ACS Omega* 5 (12) (2020) 6566–6575.
- [44] L.L. Xiong, R. Huang, H.H. Chai, L. Yu, C.M. Li, Facile Synthesis of Fe<sub>3</sub>O<sub>4</sub>@Tannic Acid@Au Nanocomposites as a Catalyst for 4-Nitrophenol and Methylene Blue Removal, *ACS Omega* 5 (33) (2020) 20903–20911.
- [45] T. Chen, R. Huang, J. Liang, B.o. Zhou, X.-L. Guo, X.-C. Shen, B.-P. Jiang, Natural Polyphenol-Vanadium Oxide Nanozymes for Synergistic Chemodynamic/Photothermal Therapy, *Chem. Eur. J.* 26 (66) (2020) 15159–15169.
- [46] B.o. Yang, S. Zhou, J. Zeng, L. Zhang, R. Zhang, K. Liang, L. Xie, B. Shao, S. Song, G. Huang, D. Zhao, P.u. Chen, B. Kong, Super-assembled core-shell mesoporous silica-metal-phenolic network nanoparticles for combinatorial photothermal therapy and chemotherapy, *Nano Res.* 13 (4) (2020) 1013–1019.
- [47] Z.Q. Wang, Y.Q. Guo, Y. Fan, J.W. Chen, H. Wang, M.W. Shen, X.Y. Shi, Metal-Phenolic-Network-Coated Dendrimer-Drug Conjugates for Tumor MR Imaging and Chemo/Chemodynamic Therapy via Amplification of Endoplasmic Reticulum Stress, *Adv. Mater.* 34 (2022) 2107009.
- [48] Y.L. Zhang, K.Y. Xi, X. Fu, H.F. Sun, H. Wang, D.X. Yu, Z.W. Li, Y. Ma, X.J. Liu, B. Huang, S. Wang, G. Li, J.W. Cui, X.G. Li, S.L. Ni, Versatile metal-phenolic network nanoparticles for multitargeted combination therapy and magnetic resonance tracing in glioblastoma, *Biomaterials* 278 (2021), 121163.
- [49] P. Liu, X. Shi, S. Zhong, Y. Peng, Y. Qi, J. Ding, W. Zhou, Metal-phenolic networks for cancer theranostics, *Biomater. Sci.* 9 (8) (2021) 2825–2849.
- [50] Q.G. Li, Z.L. Dong, M.W. Chen, L.Z. Feng, Phenolic molecules constructed nanomedicine for innovative cancer treatment, *Coord. Chem. Rev.* 439 (2021), 213912.
- [51] Z. Guo, W. Xie, J. Lu, X. Guo, J. Xu, W. Xu, Y. Chi, N. Takuya, H. Wu, L. Zhao, Tannic acid-based metal phenolic networks for bio-applications: a review, *J. Mater. Chem. B* 9 (20) (2021) 4098–4110.
- [52] W.S. Xie, Z.H. Guo, L.Y. Zhao, Y. Wei, Metal-phenolic networks: facile assembled complexes for cancer theranostics, *Theranostics* 11 (2021) 6407–6426.
- [53] O. Mitsunobu, M. Yamada, Preparation of Esters of Carboxylic and Phosphoric Acid via Quaternary Phosphonium Salts, *Bull. Chem. Soc. Jpn.* 40 (10) (1967) 2380–2382.
- [54] B. Liu, W. Zhang, F. Yang, H. Feng, X. Yang, Facile Method for Synthesis of Fe<sub>3</sub>O<sub>4</sub>@Polymer Microspheres and Their Application As Magnetic Support for Loading Metal Nanoparticles, *J. Phys. Chem. C* 115 (32) (2011) 15875–15884.
- [55] J. Qin, G. Liang, B. Feng, G. Wang, N.a. Wu, Y. Deng, A.A. Elzatahry, A. Alghamdi, Y. Zhao, J. Wei, Facile synthesis of metal-polyphenol-formaldehyde coordination polymer colloidal nanoparticles with sub-50 nm for T<sub>1</sub>-weighted magnetic resonance imaging, *Chin. Chem. Lett.* 32 (2) (2021) 842–848.
- [56] J. Qin, G. Liang, Y. Feng, B. Feng, G. Wang, N.a. Wu, Y. Zhao, J. Wei, Synthesis of gadolinium/iron-bimetal-phenolic coordination polymer nanoparticles for theranostic applications, *Nanoscale* 12 (10) (2020) 6096–6103.
- [57] C. Chen, X.-W. Geng, Y.-H. Pan, Y.-N. Ma, Y.-X. Ma, S.-Z. Gao, X.-J. Huang, Synthesis and characterization of tannic acid-PEG hydrogel via Mitsunobu polymerization, *RSC Adv.* 10 (3) (2020) 1724–1732.
- [58] R. Ma, C. Levard, S.M. Marinakos, Y. Cheng, J. Liu, F.M. Michel, G.E. Brown, G. V. Lowry, Size-Controlled Dissolution of Organic-Coated Silver Nanoparticles, *Environ. Sci. Technol.* 46 (2) (2012) 752–759.
- [59] T.S. Peretyazhko, Q. Zhang, V.L. Colvin, Size-Controlled Dissolution of Silver Nanoparticles at Neutral and Acidic pH Conditions: Kinetics and Size Changes, *Environ. Sci. Technol.* 48 (20) (2014) 11954–11961.
- [60] H. Zhang, B. Chen, J.F. Banfield, Particle Size and pH Effects on Nanoparticle Dissolution, *J. Phys. Chem. C* 114 (35) (2010) 14876–14884.
- [61] J.-G. Kang, B.-K. Min, Y. Sohn, Synthesis and characterization of Gd(OH)<sub>3</sub> and Gd<sub>2</sub>O<sub>3</sub> nanorods, *Ceram. Int.* 41 (1) (2015) 1243–1248.
- [62] S. Hazarika, N. Paul, D. Mohanta, Rapid hydrothermal route to synthesize cubic-phase gadolinium oxide nanorods, *Bull. Mater. Sci.* 37 (4) (2014) 789–796.
- [63] B. Zhang, H. Jin, Y. Li, B. Chen, S. Liu, D. Shi, Bioinspired synthesis of gadolinium-based hybrid nanoparticles as MRI blood pool contrast agents with high relaxivity, *J. Mater. Chem.* 22 (2012) 14494–14501.
- [64] M.W. Marashdeh, B. Ababneh, O.M. Lemine, A. Alsadig, K. Omri, L. El Mir, A. Suleiman, E. Mattar, The significant effect of size and concentrations of iron oxide nanoparticles on magnetic resonance imaging contrast enhancement, *Results Phys.* 15 (2019), 102651.
- [65] K. Ranozsek-Soliwoda, E. Tomaszewska, E. Socha, P. Krzyczmonik, A. Ignaczak, P. Orlowski, M. Krzyzowska, G. Celichowski, J. Grobelny, The role of tannic acid and sodium citrate in the synthesis of silver nanoparticles, *J. Nanopart. Res.* 19 (2017) 273.
- [66] L. Falcão, M.E.M. Araújo, Application of ATR-FTIR spectroscopy to the analysis of tannins in historic leathers: The case study of the upholstery from the 19<sup>th</sup> century Portuguese Royal Train, *Vib. Spectrosc.* 74 (2014) 98–103.
- [67] D. Leibig, A.-K. Lange, A. Birke, H. Frey, Capitalizing on Protecting Groups to Influence Vinyl Catechol Monomer Reactivity and Monomer Gradient in Carbanionic Copolymerization, *Macromol. Chem. Phys.* 218 (2017) 1600553.
- [68] H. Veisi, M. Pirhayati, A. Kakanejadifard, P. Mohammadi, M.R. Abdi, J. Gholami, S. Hemmati, In Situ Green Synthesis of Pd Nanoparticles on Tannic Acid-Modified Magnetite Nanoparticles as a Green Reductant and Stabilizer Agent: Its Application as a Recyclable Nanocatalyst (Fe<sub>3</sub>O<sub>4</sub>@TA/Pd) for Reduction of 4-Nitrophenol and Suzuki Reactions, *ChemistrySelect* 3 (2018) 1820–1826.
- [69] J.J. Dolo, H.C. Swart, E. Coetsee, J.J. Terblans, O.M. Ntwaeaborwa, B.F. Dejene, XPS analysis and luminescence properties of thin films deposited by the pulsed laser deposition technique, *Hyperfine Interact.* 197 (1-3) (2010) 129–134.
- [70] A. Saha, S.C. Mohanta, K. Deka, P. Deb, P.S. Devi, Surface-Engineered Multifunctional Eu:Gd<sub>2</sub>O<sub>3</sub> Nanoplates for Targeted and pH-Responsive Drug Delivery and Imaging Applications, *ACS Appl. Mater. Interfaces* 9 (2017) 4126–4141.
- [71] T. Tegafaw, W. Xu, M.W. Ahmad, J.S. Baeck, Y. Chang, J.E. Bae, K.S. Chae, T. J. Kim, G.H. Lee, Dual-mode T<sub>1</sub> and T<sub>2</sub> magnetic resonance imaging contrast agent based on ultrasmall mixed gadolinium-dysprosium oxide nanoparticles: synthesis, characterization, and *in vivo* application, *Nanotechnology* 26 (2015), 365102.
- [72] Y. Luo, A. Habrioux, L. Calvillo, G. Granozzi, N. Alonso-Vante, Yttrium Oxide/Gadolinium Oxide-Modified Platinum Nanoparticles as Cathodes for the Oxygen Reduction Reaction, *ChemPhysChem* 15 (10) (2014) 2136–2144.
- [73] P.Z. Si, I. Škorvánek, J. Kováč, D.Y. Geng, X.G. Zhao, Z.D. Zhang, Structure and magnetic properties of Gd nanoparticles and carbon coated Gd/GdC<sub>2</sub> nanocapsules, *J. Appl. Phys.* 94 (10) (2003) 6779–6784.
- [74] N. Ullah, M. Imran, K. Liang, C.-Z. Yuan, A. Zeb, N. Jiang, U.Y. Qazi, S. Sahar, A.-W. Xu, Highly dispersed ultra-small Pd nanoparticles on gadolinium hydroxide nanorods for efficient hydrogenation reactions, *Nanoscale* 9 (36) (2017) 13800–13807.
- [75] F. Chen, X.H. Zhang, X.D. Hu, W. Zhang, R. Zeng, P.D. Liu, H.Q. Zhang, Synthesis and characteristics of nanorods of gadolinium hydroxide and gadolinium oxide, *J. Alloy. Compd.* 664 (2016) 311–316.
- [76] R. Priya, O.P. Pandey, S.J. Dhoble, Review on the synthesis, structural and photo-physical properties of Gd<sub>2</sub>O<sub>3</sub> phosphors for various luminescent applications, *Opt. Laser Technol.* 135 (2021), 106663.
- [77] M.S. de Almeida, M.A.B. dos Santos, R.D. Goncalves, M.R.D. Santos, A.P. D. Marques, E. Longo, F.D. La Porta, I.M. Pinatti, M.D.P. Silva, M.J. Godinho, Novel Gd(OH)<sub>3</sub>, GdOOH and Gd<sub>2</sub>O<sub>3</sub> Nanorods: Microwave-Assisted Hydrothermal Synthesis and Optical Properties, *Mater. Res.* 19 (2016) 1155–1161.
- [78] D. Raiser, J.P. Deville, Study of XPS photoemission of some gadolinium compounds, *J. Electron Spectrosc. Relat. Phenom.* 57 (1) (1991) 91–97.
- [79] A.P. Jadhav, J.H. Oh, S.W. Park, H. Choi, B.K. Moon, B.C. Choi, K. Jang, J. H. Jeong, S.S. Yi, J.H. Kim, Enhanced down and upconversion emission for Li<sup>+</sup> co-doped Gd<sub>2</sub>O<sub>3</sub>:Er<sup>3+</sup> nanostructures, *Curr. Appl. Phys.* 16 (10) (2016) 1374–1381.
- [80] Z.A. Taha, A. Ajlouni, A.K. Hijazi, F.E. Kühn, E. Herdtweck, Redetermination of [Gd(NO<sub>3</sub>)<sub>3</sub>(H<sub>2</sub>O)<sub>4</sub>]•2H<sub>2</sub>O, *Acta Cryst. E* 68 (2012) i56–i57.

## SUPPORTING INFORMATION

### Hybrid Polyphenolic Network/SPIONs Aggregates with Potential Synergistic Effects in MRI Applications

A. Lazzarini<sup>a,\*</sup>, R. Colaiezzi<sup>a</sup>, A. Galante<sup>b,c,d</sup>, M. Passacantando<sup>a</sup>, D. Capista<sup>a</sup>, F. Ferella<sup>a,c</sup>, M. Alecci<sup>b,c,d</sup>, M. Crucianelli<sup>a,\*</sup>

<sup>a</sup> *Department of Physical and Chemical Sciences, University of L'Aquila, Via Vetoio (COPPITO 1-2), 67100, L'Aquila - Italy.*

<sup>b</sup> *Department of Life, Health and Environmental Sciences, University of L'Aquila, Via Vetoio (COPPITO 2), 67100, L'Aquila - Italy.*

<sup>c</sup> *INFN Gran Sasso National Laboratories, Via G. Acitelli 22, 67100, Assergi (AQ) - Italy.*

<sup>d</sup> *Institute for Superconductors, Oxides and Other Innovative Materials and Devices, National Research Council, Via Vetoio 1, 67100 L'Aquila - Italy.*

\* *Corresponding authors: [andrea.lazzarini@univaq.it](mailto:andrea.lazzarini@univaq.it); [marcello.crucianelli@univaq.it](mailto:marcello.crucianelli@univaq.it)*

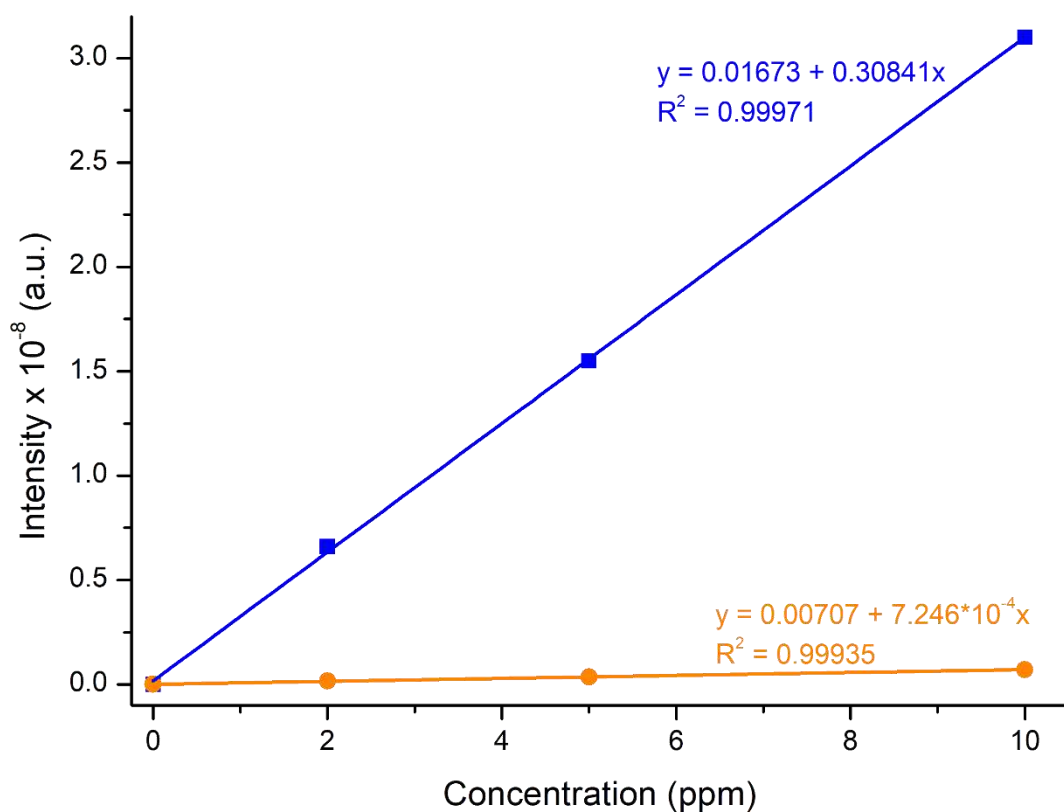


**Figure S1.** ICP-MS calibration curves for <sup>56</sup>Fe (blue) and <sup>57</sup>Fe (orange) isotopes.

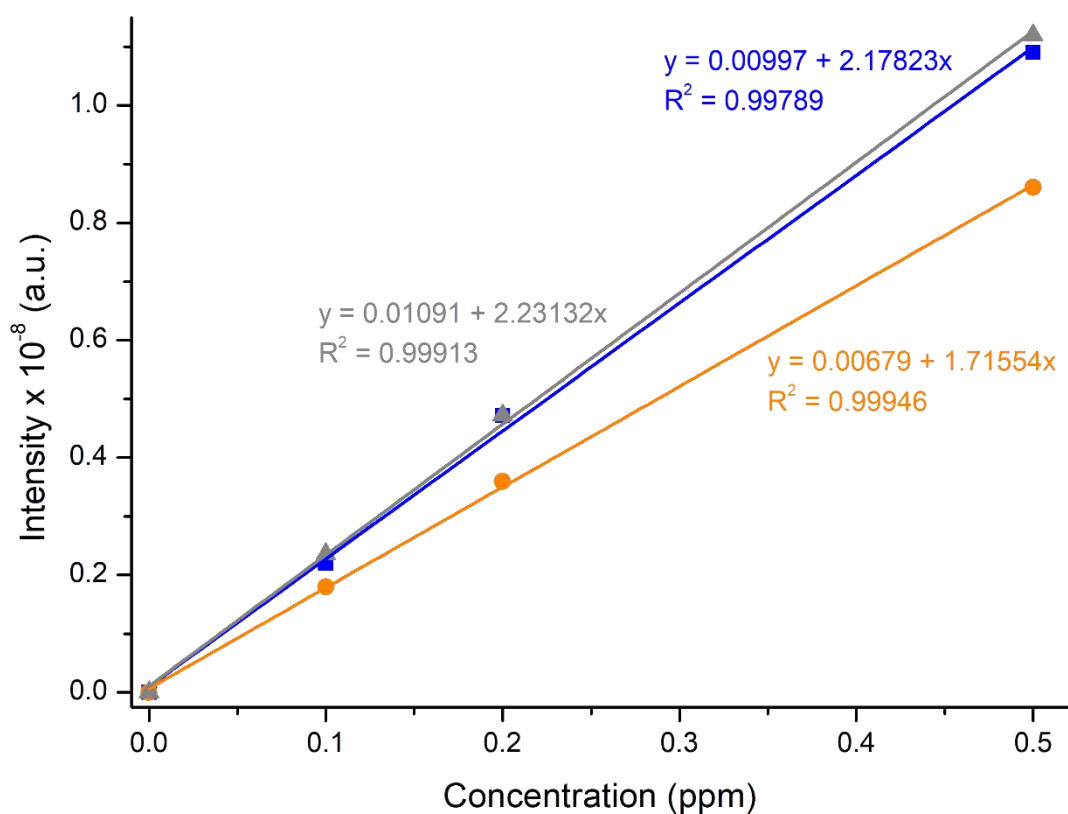


**Figure S2.** ICP-MS calibration curves for <sup>156</sup>Gd (blue), <sup>157</sup>Gd (orange) and <sup>158</sup>Gd (grey) isotopes.

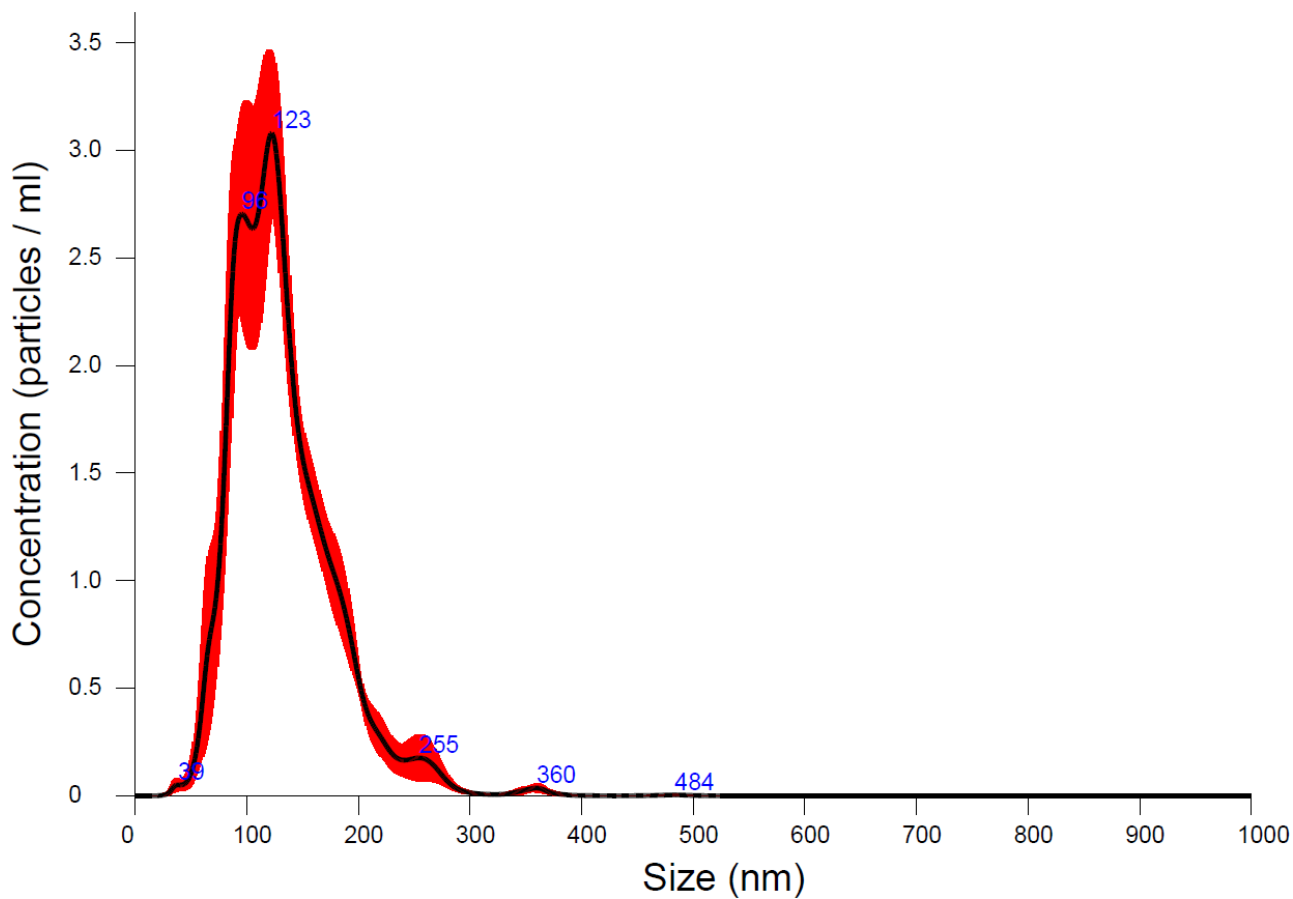


Figure S3. Particle size distribution for sample SPIONs.

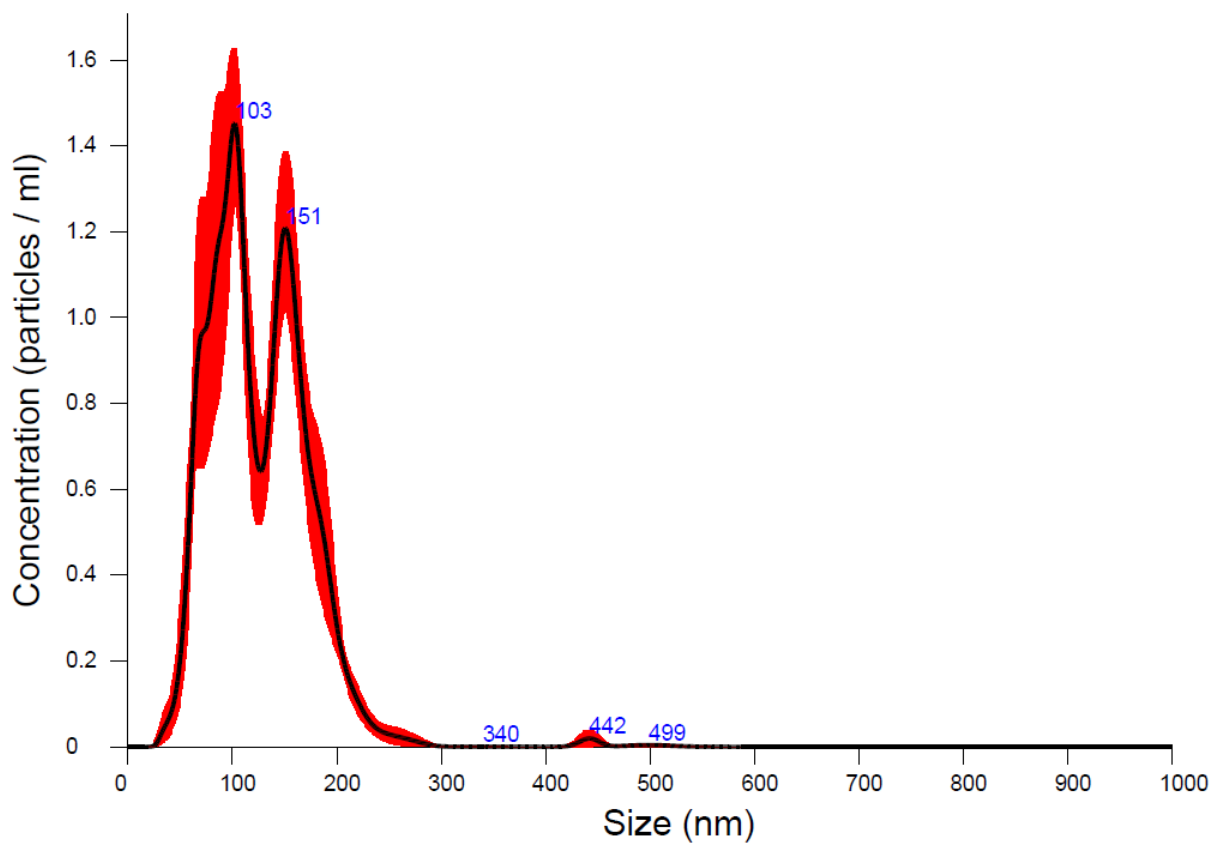


Figure S4. Particle size distribution for sample A<sub>1</sub>.

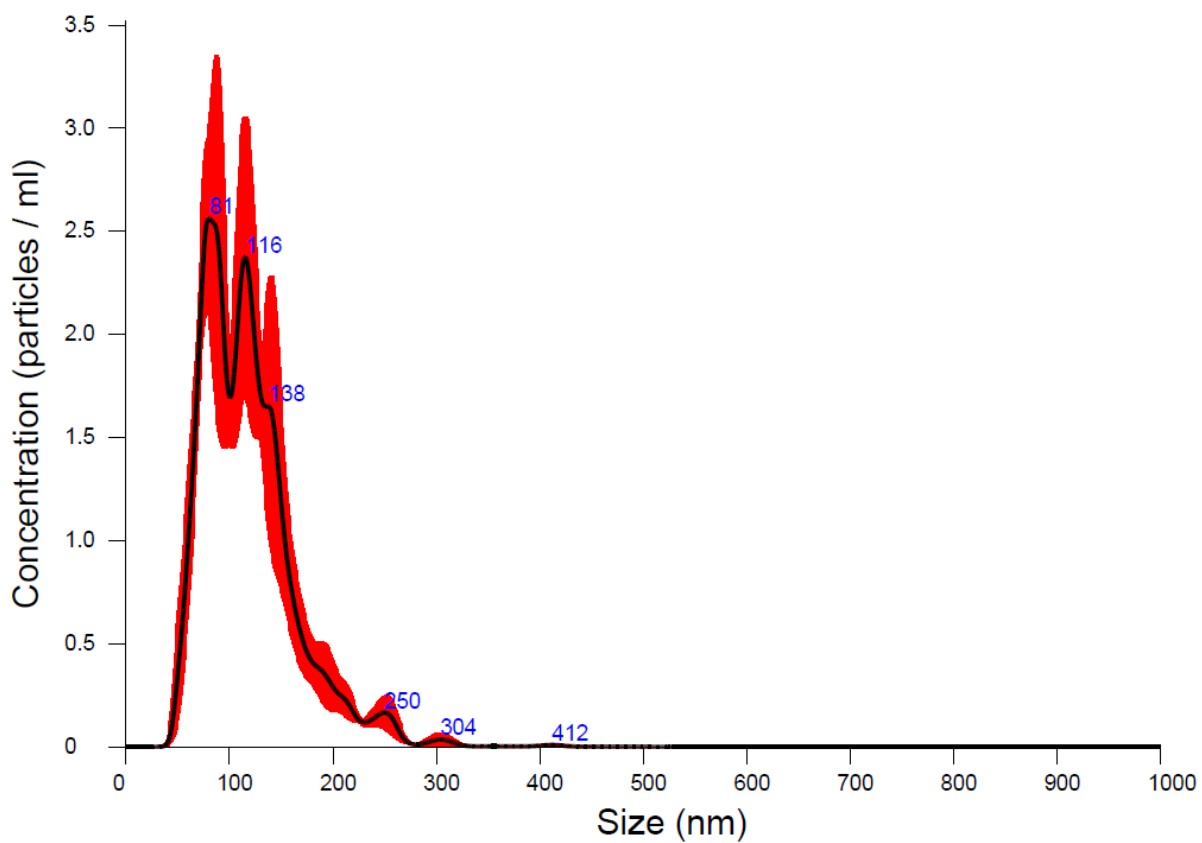


Figure S5. Particle size distribution for sample A<sub>2</sub>.

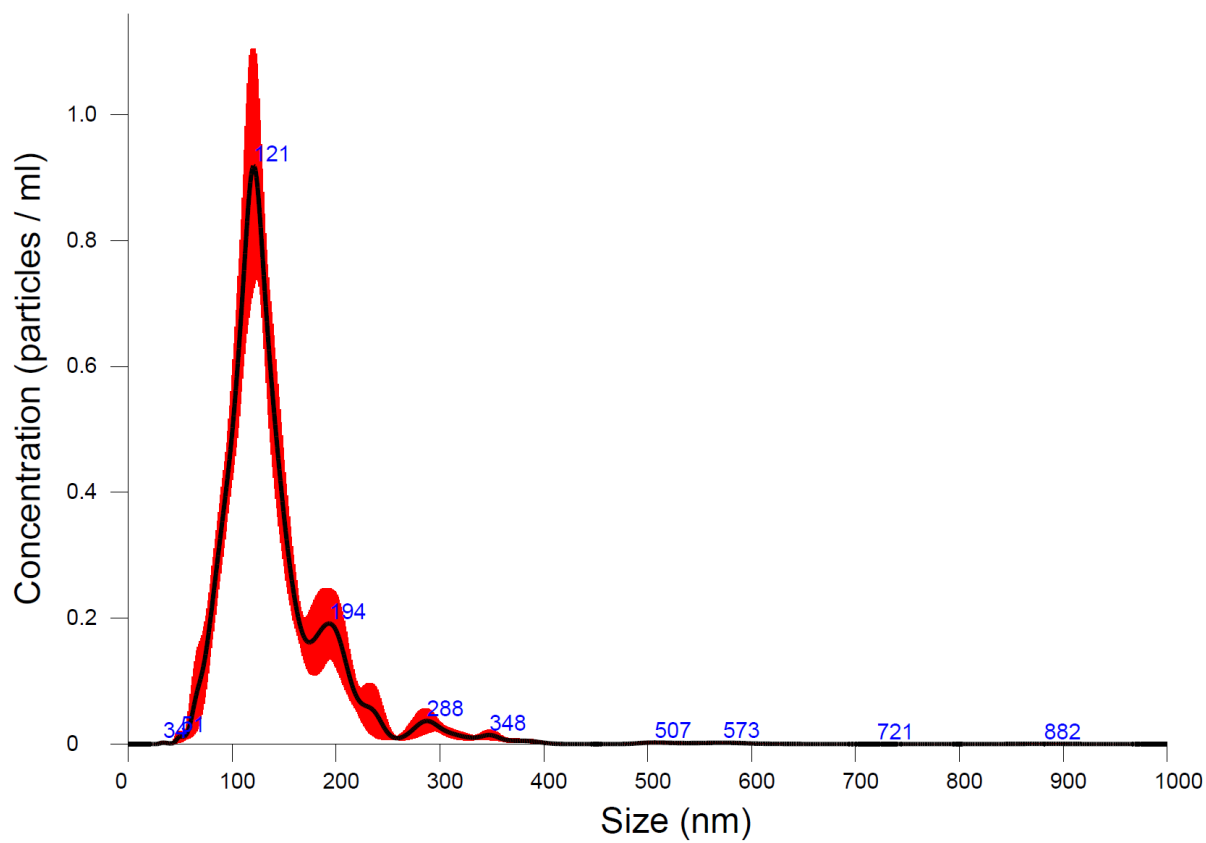
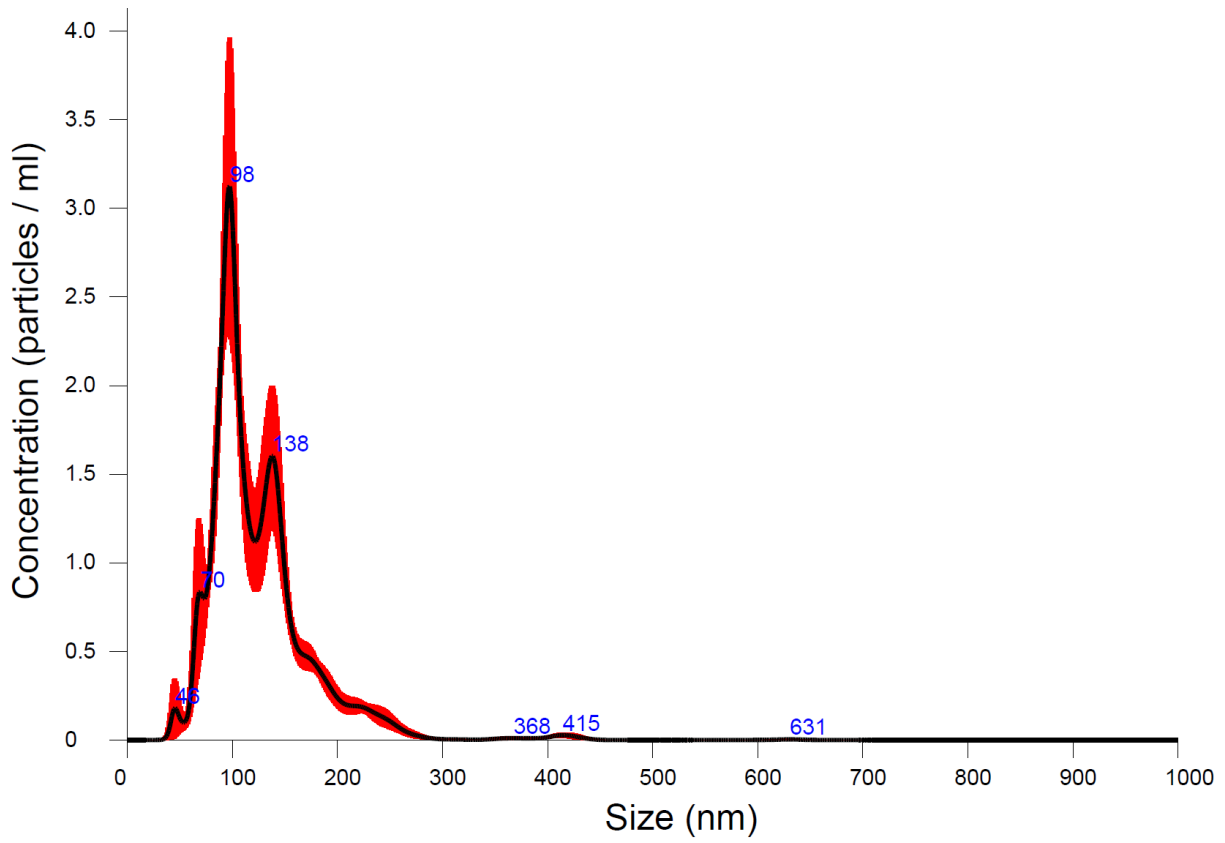
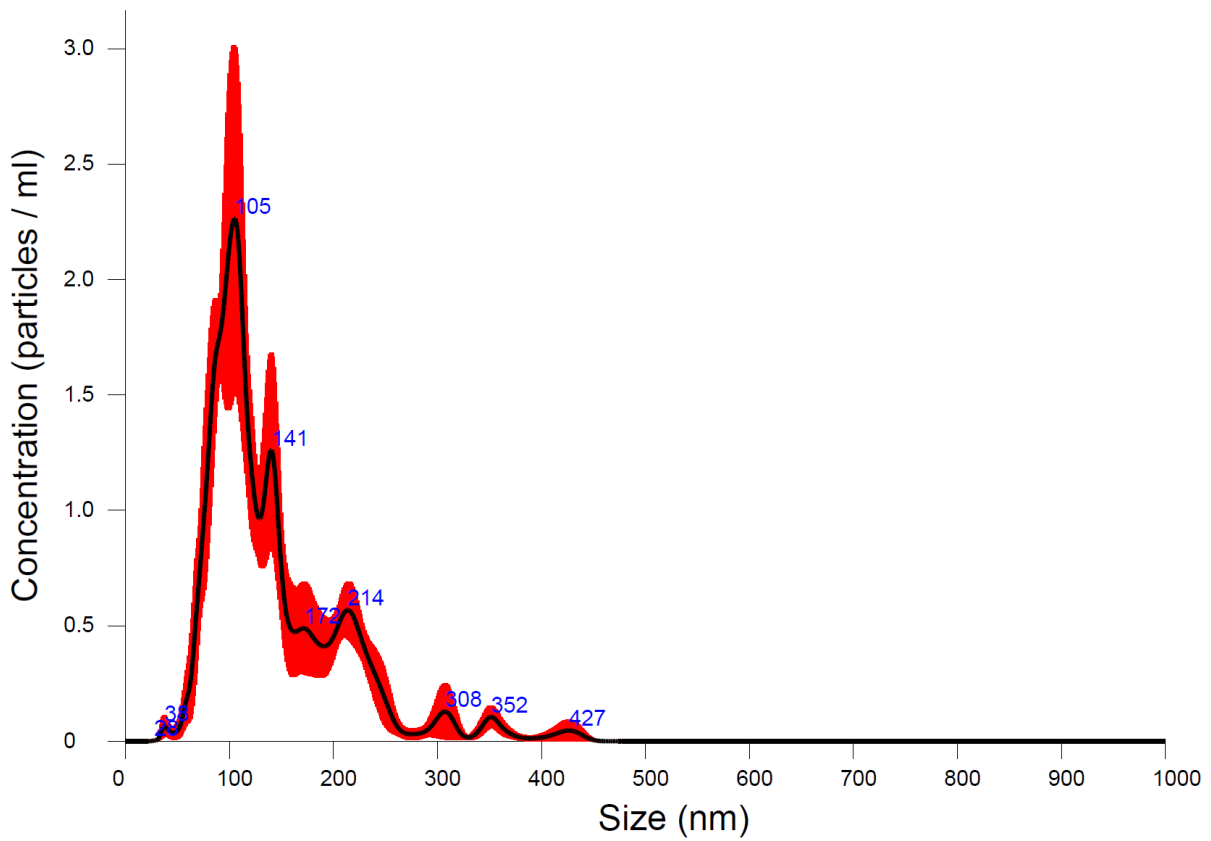


Figure S6. Particle size distribution for sample B<sub>1</sub>.



**Figure S7.** Particle size distribution for sample B<sub>2</sub>.



**Figure S8.** Particle size distribution for sample B<sub>3</sub>.

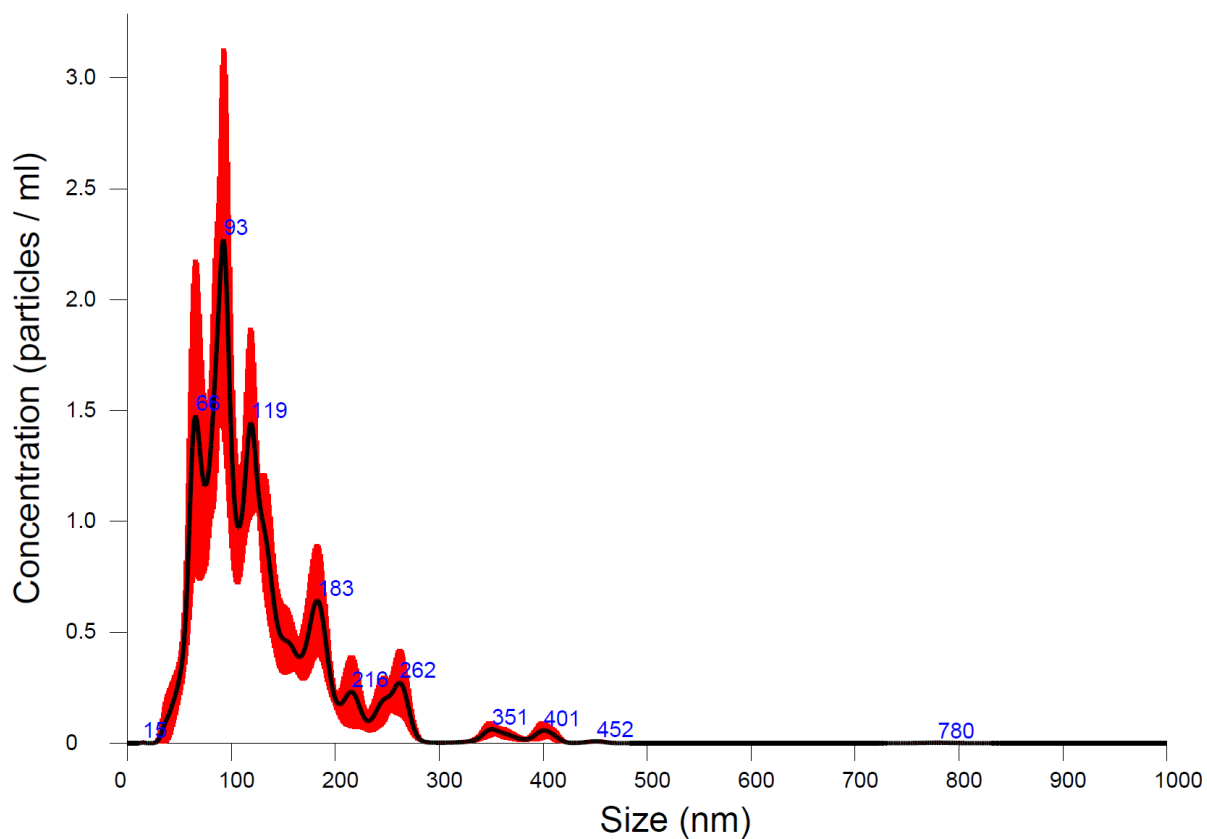


**Figure S9.** Particle size distribution for sample B<sub>4</sub>.

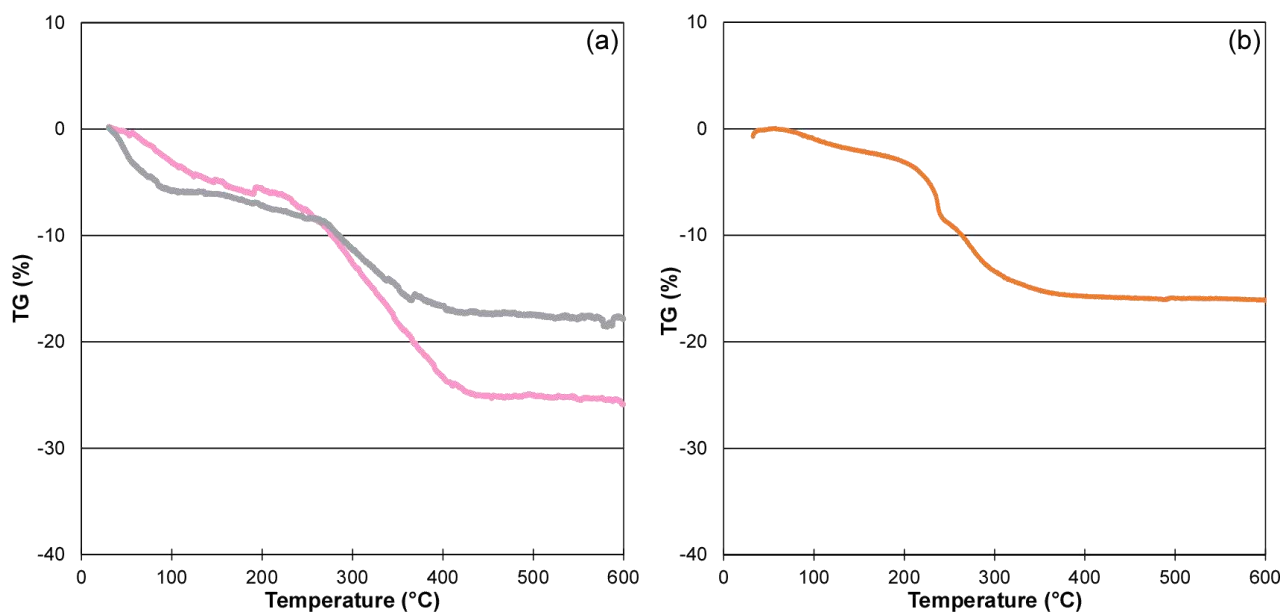


**Figure S10.** Part a) Thermogravimetric curve for samples A<sub>1</sub> (pink line) and A<sub>2</sub> (grey line). Part b) Thermogravimetric curve for sample B<sub>1</sub>.

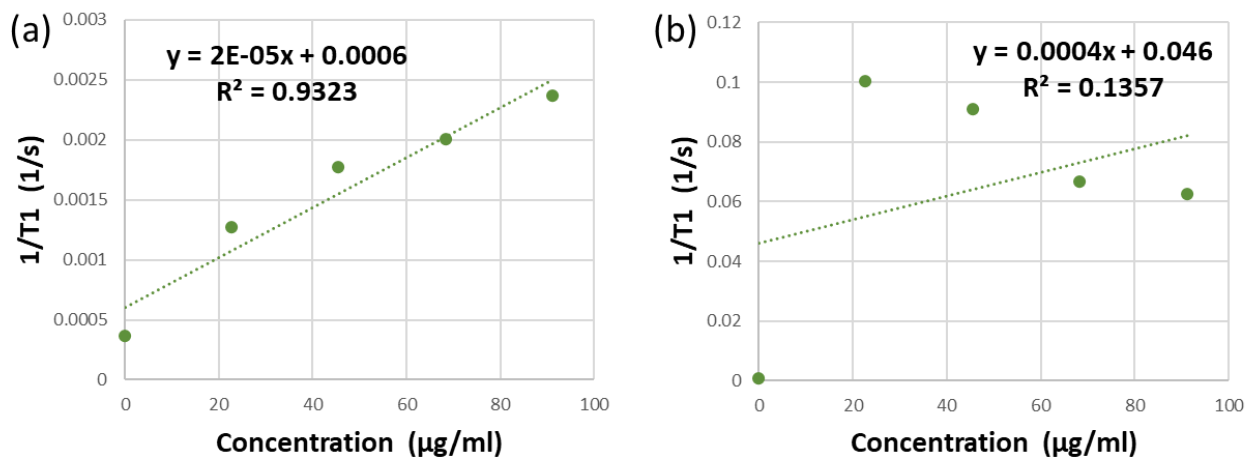


Figure S11. Relaxivity measurements for sample SPIONs. Part (a) shows R<sub>1</sub> trend; part (b) shows R<sub>2</sub> trend.

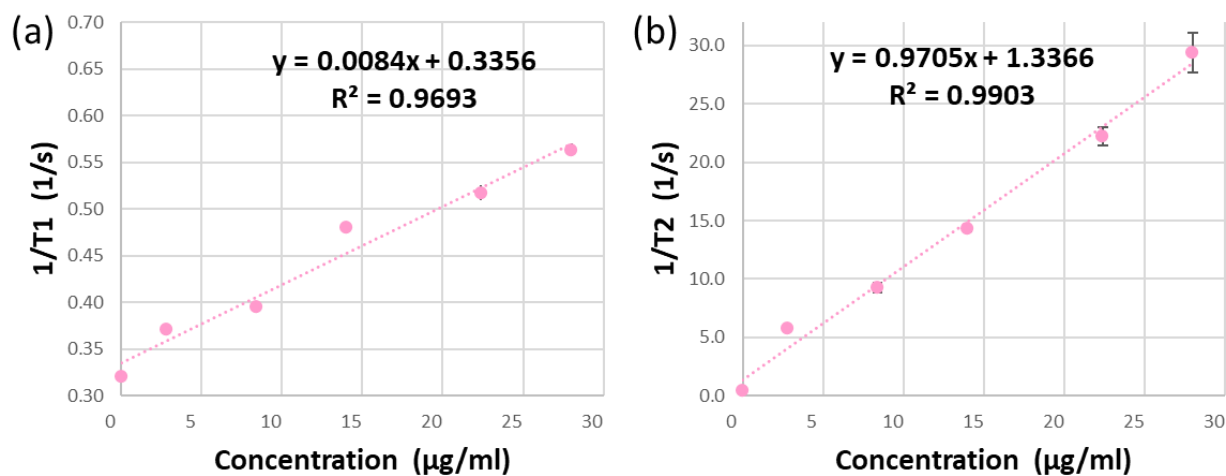


Figure S12. Relaxivity measurements for sample A<sub>1</sub>. Part (a) shows R<sub>1</sub> trend; part (b) shows R<sub>2</sub> trend.

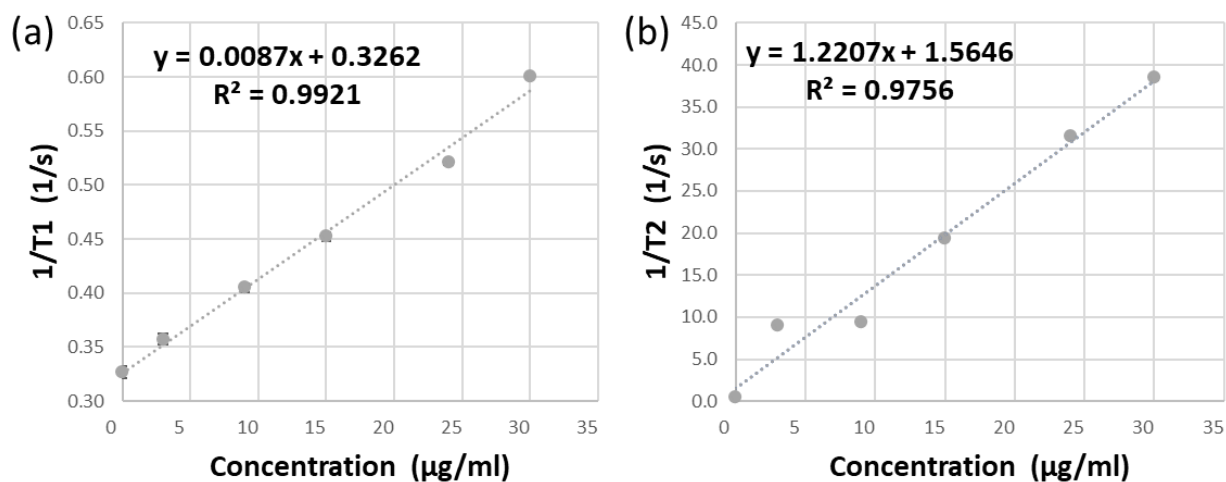


Figure S13. Relaxivity measurements for sample A<sub>2</sub>. Part (a) shows R<sub>1</sub> trend; part (b) shows R<sub>2</sub> trend.

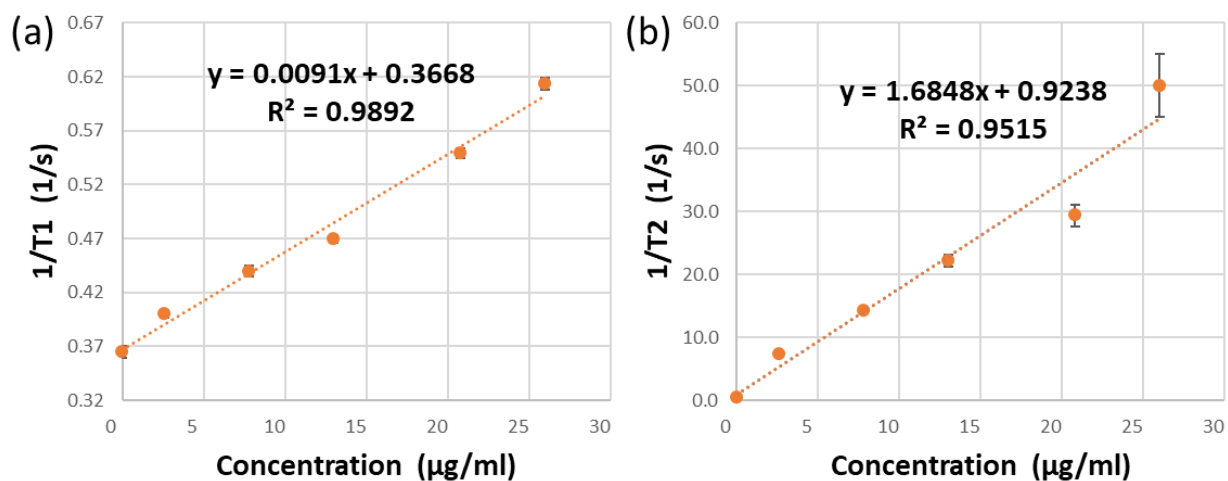


Figure S14. Relaxivity measurements for sample B<sub>1</sub>. Part (a) shows R<sub>1</sub> trend; part (b) shows R<sub>2</sub> trend.

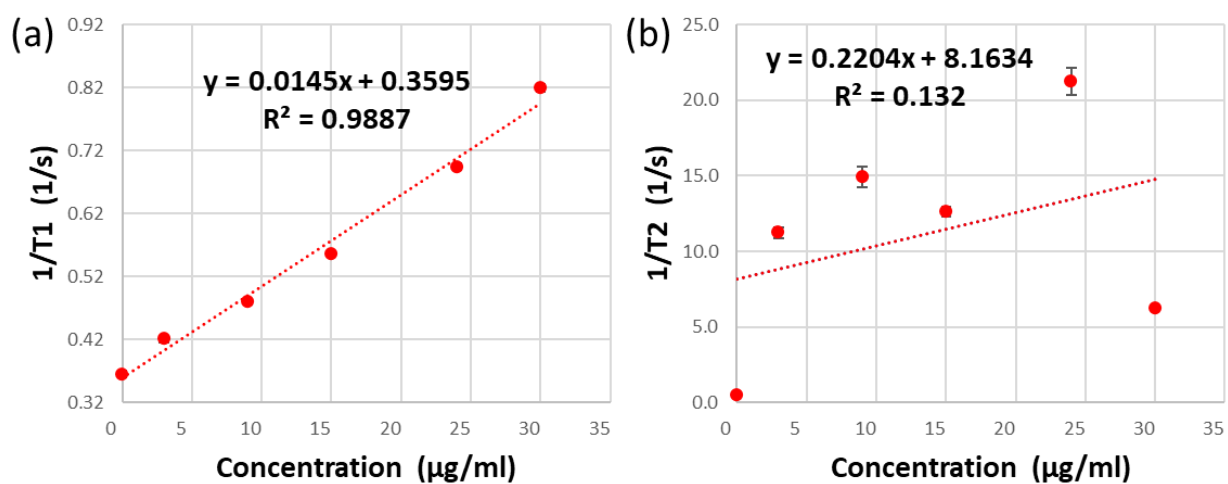
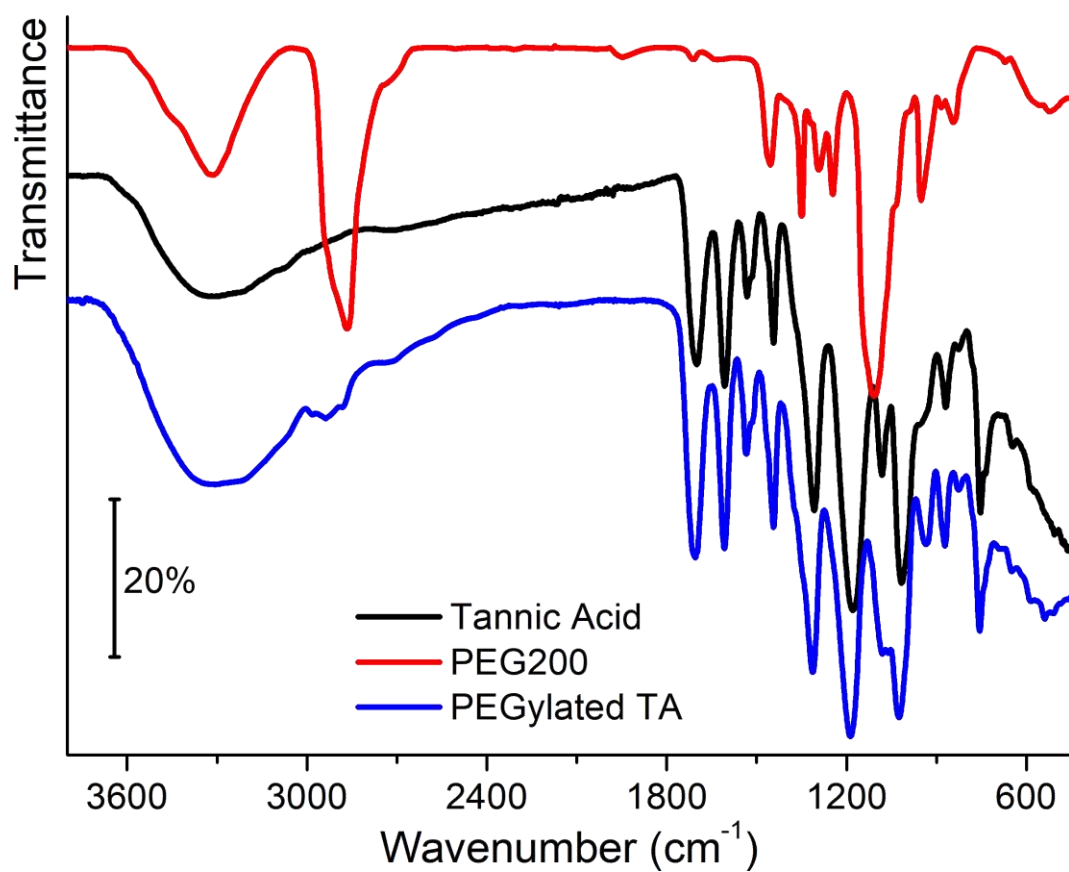
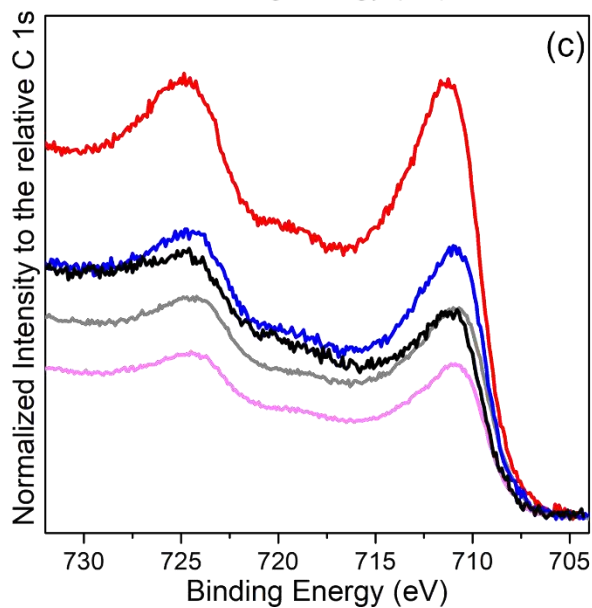
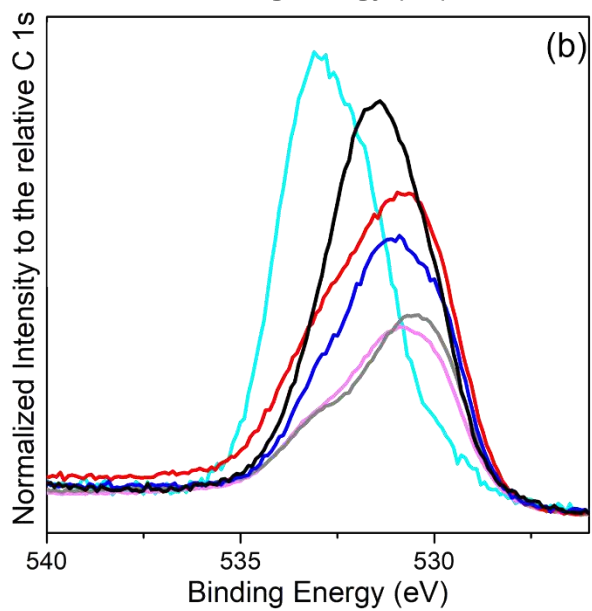
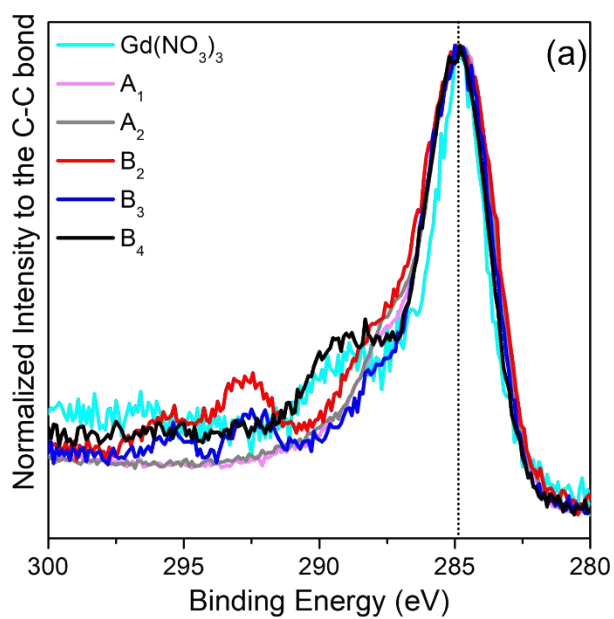


Figure S15. Relaxivity measurements for sample B<sub>2</sub>. Part (a) shows R<sub>1</sub> trend; part (b) shows R<sub>2</sub> trend.



**Figure S16.** ATR-IR spectra of Tannic Acid (black), PEG200 (red) and PEGylated Tannic Acid (blue).



**Figure S17.** C 1s (part a), O 1s (part b) and Fe 2p (part c) XPS spectra for Gd(NO<sub>3</sub>)<sub>3</sub> (light blue curve), and for samples A<sub>1</sub> (pink curve), A<sub>2</sub> (grey curve), B<sub>2</sub> (red curve), B<sub>3</sub> (blue curve), B<sub>4</sub> (black curve).